

Abstract

Rationale: Renal fibrosis, with no therapeutic approaches, is a common pathological feature in various chronic kidney diseases (CKD). Tubular cell injury plays a pivotal role in renal fibrosis. Commonly, injured tubular cells exhibit significant lipid accumulation. However, the underlying mechanisms remain poorly understood.

Methods: 2-arachidonoylglycerol (2-AG) levels in CKD patients and CKD model specimens were measured using mass spectrometry. 2-AG-loaded nanoparticles were infused into unilateral ureteral obstruction (UUO) mice. Lipid accumulation and renal fibrosis were tested. Furthermore, monoacylglycerol lipase (MAGL), the hydrolyzing enzyme of 2-AG, was assessed in CKD patients and models. Tubular cell-specific MAGL knock-in mice were generated. Moreover, MAGL recombination protein was also administered to unilateral ischemia reperfusion injury (UIRI) mice. Besides, a series of methods including RNA sequencing, metabolomics, primary cell culture, lipid staining, etc. were used.

Results: 2-AG was increased in the serum or kidneys from CKD patients and models. Supplement of 2-AG further induced lipid accumulation and fibrogenesis through cannabinoid receptor type 2 (CB2)/ β -catenin signaling. β -catenin knockout blocked 2-AG/CB2-induced fatty acid β -oxidation (FAO) deficiency and lipid accumulation. Remarkably, MAGL significantly decreased in CKD, aligning with lipid accumulation and fibrosis. Specific transgene of MAGL in tubular cells significantly preserved FAO, inhibited lipid-mediated toxicity in tubular cells, and finally retarded fibrogenesis. Additionally, supplementation of MAGL in UIRI mice also preserved FAO function, inhibited lipid accumulation, and protected against renal fibrosis.

49 Conclusion: MAGL is a potential diagnostic marker for kidney function decline, and also serves
50 as a new therapeutic target for renal fibrosis through ameliorating lipotoxicity.

51

52 Keywords: MAGL; lipotoxicity; renal fibrosis; 2-AG; FAO

53

54

55

56

57

58

59

60

61

62

63

64

65

Introduction

The prevalence of CKD is increasing worldwide, with rates ranging from 8% to 16% [1]. Tubulointerstitial fibrosis, a common pathological feature of CKD, is a significant risk factor for the high morbidity and mortality associated with the disease [2,3]. Unfortunately, early detection of renal fibrosis remains challenging, and effective treatment options are currently lacking [4]. Therefore, it is crucial to understand the mechanisms underlying renal fibrosis in order to develop early diagnostic methods and effective therapeutic interventions for CKD. Renal epithelial cell is a major component of kidney. Renal fibrosis is closely associated with tubular cell injury [5–7]. These cells have a high metabolic rate and require a significant energy supply. To meet this demand, renal epithelial cells rely on FAO, an oxygen-dependent metabolic process that occurs within the mitochondria, to generate adenosine triphosphate (ATP) [8,9]. FAO involves the degradation of fatty acids to produce energy [10,11].

Kidney is the second-highest organ with mitochondrial abundance, which almost exclusively relies on FAO for ATP production [12,13]. Lipid droplets play key roles in maintaining lipid balance, but excessive lipid accumulation in cells leads to lipotoxicity, meaning that the accumulation of lipid intermediates or metabolites impairs cell functions [14–16]. In renal tubular cells, decreased lipid metabolism results in lipid droplet accumulation and further induces lipotoxicity [17]. Maintaining lipid homeostasis in kidney is crucial for meeting energy demands [18]. However, in kidney injury, fatty acid utilization is disrupted, leading to lipid accumulation and subsequent lipotoxicity damages, characterized by mitochondrial impairment, endoplasmic reticulum stress, and increased reactive oxygen species production, etc. [19–22]. Numerous studies have confirmed that lipotoxicity plays a key role in renal fibrosis [23–25].

Key regulators of FAO-related gene transcription are peroxisome proliferator-activated receptor alpha (PPAR α) and peroxisome proliferator-activated receptor gamma coactivator-1 alpha (PGC-1 α) [23,26,27]. Previous researches have demonstrated that decreased levels of PPAR α and PGC-1 α contribute to FAO dysfunction and the formation of lipid droplets in renal tubular cells, leading to the development of renal fibrosis [23,26,28]. Interestingly, studies, including our own, have shown that β -catenin regulates PGC-1 α [29]. However, the potential role of β -catenin in modulating FAO dysfunction requires further investigation.

The endocannabinoid system (ECS) is composed of receptors, specifically cannabinoid receptor 1 and 2 (CB1 and CB2), endogenous ligands referred to as endocannabinoids (primarily 2-AG and Anandamide), and enzymes responsible for metabolizing these ligands [30]. Previous studies have indicated that CB2/ β -catenin plays a crucial role in tubular cell injury and renal fibrosis [31,32]. Additionally, the downregulation of PGC-1 α in aging kidneys has been linked to the ECS [33]. These findings suggest a potential involvement of the ECS and its downstream pathways in the dysregulation of FAO. However, further investigation is required to fully comprehend the precise mechanisms. Of note, a previous report showed the level of 2-AG was increased in kidneys of UUO [34], suggesting 2-AG/CB2 could be involved in energy metabolism in renal fibrosis. However, this should be clarified. Furthermore, MAGL is a major enzyme of ECS and responsible for the degradation of 85% of 2-AG [35]. MAGL is a 33 kDa serine hydrolase, which can decompose monoacylglycerols into fatty acid and glycerol [36]. As a comprehensive metabolic center, MAGL can also regulate lipid signaling transduction [37]. However, the role of MAGL has not been elucidated in kidney area.

In this study, we discovered that 2-AG promotes lipid accumulation and fibrogenesis in renal

tubular cell through β -catenin signaling. Our findings provide an insightful view of the endocannabinoid system in the kidney area and suggest MAGL is a promising strategy for treating CKD. We also found MAGL hydrolyzes 2-AG and decreases in clinical patients and CKD models. Supplementation of MAGL effectively ameliorates FAO dysfunction and retards renal fibrosis. MAGL could serve as a diagnostic risk factor for the decline of renal function. Furthermore, MAGL could also serve as an innovative therapeutic strategy for CKD.

Results

2-AG increases in CKD and drives lipid deposition and fibrogenesis in tubular cells

We firstly examined the levels of 2-AG in the circulation of 34 healthy individuals and 44 patients with CKD at stage 5. As depicted in Figure 1A-C, serum 2-AG exhibited a significant increase in CKD patients. The chi-square test results further confirmed a higher detection rate of 2-AG in CKD group compared to control group. We also measured 2-AG levels in the serum or kidney homogenates of UUO mice and folic acid nephropathy (FAN) mice, both of which were utilized as CKD models. Significantly elevated levels of 2-AG were observed in both groups compared to control (Figure 1D-F). Subsequently, HK-2 cells, a human proximal tubular cell line, were cultured and subjected to 2-AG treatment (Figure 1G). The findings demonstrated that the administration of 2-AG led to a reduction in ATP production, as illustrated in Figure 1H. Moreover, lipid accumulation was observed upon exposure to 2-AG (Figure 1I). Furthermore, 2-AG elicited fibrogenesis (Figure 1J-M). These findings suggest 2-AG may play a significant role in CKD, influencing disease progression and modulating lipid metabolism, fibrosis, and energy metabolism in renal tubular cells.

2-AG promotes lipid deposition and renal fibrosis in UUO mice

Liposome-nanoparticle-encapsulated 2-AG was labeled with indocyanine green (ICG) to enhance its aqueous solubility and administered to UUO mice (Figure 2A). In vivo imaging demonstrated a substantial accumulation of 2-AG in UUO-affected kidney 2 h after intravenous injection, whereas sham mice did not exhibit such accumulation (Figure 2B). Fluorescence analysis revealed that 2-AG was predominantly localized in tubules (Figure 2C), rather than in glomeruli (Figure S1A). Additionally, the 2-AG content in kidney homogenates was assessed, revealing a further increase induced by 2-AG in UUO mice (Figure 2D). We then performed RNA sequencing (Figure S1B-C). The heatmap showed 2-AG treatment increased extracellular matrix and lipid accumulation, but decreased fatty acid metabolism and mitochondrial function (Figure 2E). Gene Set Enrichment Analysis (GSEA) also revealed low enrichments of unsaturated fatty acid metabolism and upregulation of lipid complex and extracellular matrix in UUO mice with 2-AG treatment, as shown in Figure S1D-F. The co-staining showed 2-AG could be evolved by all segment of tubules (Figure 2F). We assessed the protein levels of CB2 and Active- β -catenin, and both western blot and immunofluorescence analyses revealed that 2-AG significantly upregulated their levels (Figure 2G-H and Figure S1G). Interestingly, 2-AG was highly colocalized with β -catenin expression (Figure 2I). We further conducted non-targeted metabolomics analysis in kidney tissues in both UUO and UUO/2-AG groups. The results revealed that lipids and lipid-like molecules accounted for the majority of detected substances (Figure S1H). Heatmap analysis demonstrated 2-AG induced a significant increase in medium, long as well as very long-chain fatty acids and their derivatives, such as Palmitic acid, Azelaic acid, Octanedioic acid (Figure S1I). Moreover, the transmission electron

microscopy (TEM) analysis showed 2-AG strongly induced lipid accumulation in UUO mice and also induced mild deposition of lipid in sham mice (Figure 2J). We then examined the FAO and fibrosis-related proteins. As shown in Figure 2K and Figure S1J-L, PGC-1 α , PPAR α , carnitine palmitoyl-transferase 1A (CPT1A), and acyl-CoA oxidase 1 (ACOX1) exhibited downregulation in UUO mice, and their expression was further reduced by 2-AG. Conversely, treatment with 2-AG led to an increased induction of Fibronectin, Collagen I, and Vimentin. Furthermore, fibrogenesis, lipid accumulation, and FAO function decline were also observed in UUO mice and were exacerbated by treatment with 2-AG, as shown by staining of Nile Red, adipose differentiation-related protein (ADRP, the most well-characterized membrane protein associated with lipid droplets [38]), PPAR α , CPT1A, Fibronectin and Sirius Red (Figure 2L, Figure S1M-N).

MAGL is decreased in CKD and correlated with preservation of kidney function

MAGL, an enzyme responsible for the hydrolysis of 2-AG (Figure 3A), exhibited a broad expression pattern in renal tubules as evidenced by co-staining with various tubule segment markers such as lotus tetragonolobus lectin (LTL), peanut agglutinin (PNA) and dolichos biflorus agglutinin (DBA) (Figure 3B). In order to further explore its role in kidney, we examined MAGL expression in patients at various stages of CKD. Notably, there was a significant decrease in MAGL levels in tubules as CKD progressed, as evidenced in Figure 3C-D. Additionally, we observed a similar decline pattern in urinary MAGL levels, as shown in Figure 3E. Correlation analysis demonstrated a positive relationship between MAGL expression and preservation of estimated glomerular filtration rate (eGFR) (Figure 3F), as well

as a positive correlation between urinary MAGL levels and eGFR (Figure 3G). MAGL was found to be reduced in various types of CKD (Figure 3H). We further investigated the expression of MAGL in animal models. The mRNA levels of MAGL in the kidneys of FAN and UUO mice exhibited a significant decrease (Figure 3I-J). Furthermore, in both UUO mice and adriamycin (ADR) mice models, the protein levels of MAGL exhibited a progressive decline over time, as demonstrated in Figure 3K-L and Figure S2A-D. The results suggest that MAGL serves as a prognostic factor for renal function decline in CKD.

Loss of MAGL correlates with lipid accumulation and fibrosis

The co-staining revealed a significant decrease in MAGL expression in UUO mice, accompanied by upregulation of CB2, β -catenin activation, ADRP, and Fibronectin (Figure 4A). Western blot analysis further confirmed the substantial reduction of MAGL and CPT1A expression, as well as the induction of Active β -catenin in UUO mice (Figure 4B and Figure S2E-G). Additionally, MAGL and CPT1A were demonstrated their strong expression and co-localization in control kidney, but absent in UUO (Figure S2H). The similar results were also observed in ADR and UIRI mice models (Figure S2I-Q). The correlation between MAGL and β -catenin was examined. When MAGL decreased in CKD, β -catenin increased, and a negative correlation was observed between them (Figure 4C-D). In healthy controls, MAGL widely expressed and co-localized with CPT1A, while in CKD, MAGL and CPT1A decreased (Figure 4E). A negative correlation was also observed between MAGL and ADRP (Figure 4F-G). A negative correlation was found between MAGL and injury tubules or renal fibrosis (Figure 4H-I). Moreover, co-staining of MAGL and Fibronectin showed MAGL-negative tubules were

surrounded by Fibronectin-positive fibroblasts (Figure 4J).

In vitro, MAGL was added to cell culture treated with 2-AG. The results indicated that MAGL reduced 2-AG levels by at least 50% and suppressed CB2 expression while leaving CB1 unaffected (Figure S3).

MAGL effectively inhibits TGF- β 1-induced lipotoxicity and fibrosis in tubular cells

We generated tubular cell-specific MAGL knock-in mice (MAGL-CKI) and isolated primary tubular cells from both wildtype and MAGL-CKI mice. Subsequently, these cells were stimulated with TGF- β 1 (Figure 5A-C). Our findings revealed a time-dependent reduction in MAGL protein levels in primary tubules of wildtype mice in response to TGF- β 1 (Figure 5D-E). Western blot analysis revealed that MAGL-CKI successfully inhibited the increased expression of CB2 and Active- β -catenin induced by TGF- β 1 (Figure 5F-G). Additionally, MAGL-CKI reversed the decrease in FAO levels induced by TGF- β 1 and mitigated the expression of Fibronectin (Figure 5H-L). The efficacy of MAGL-CKI in reducing lipid deposition and fibrosis was further validated through fluorescence staining (Figure 5M). In addition to isolate primary cells, we further validated our findings by applying MAGL recombinant protein to HK-2 cells. Significantly, the consistent application of MAGL effectively mitigated TGF- β 1-induced alterations, including lipid deposition, fibrosis, activation of CB2/ β -catenin, and reduced FAO levels (Figure 5N-W). Similarly, the MAGL inhibitor JZL-184 demonstrated opposite effects. (Figure S4).

Tubular cell specific MAGL knock-in mice inhibit CB2/ β -catenin signaling

These mice were viable, fertile, and indistinguishable from WT littermates. MAGL knock-

in did not affect FAO levels or mitochondrial functions, and no changes in lipid accumulation or fibrosis were observed after MAGL knock-in (Figure S5). FAN model was constructed in MAGL knock-in mice (Figure 6A). The effectiveness of transgene expression was determined by MAGL mRNA and protein levels (Figure 6B-E). Renal function indexes, serum creatinine (Scr), and blood urea nitrogen (BUN), were increased in FAN mice but greatly decreased in MAGL-CKI mice (Figure 6F-G). Notably, MAGL knock-in also reduced 2-AG contents in kidney homogenates (Figure 6H). RNA sequencing showed downregulated fibrosis-related genes, but upregulated FAO-related genes and lipid oxidation in MAGL-CKI mice (Figure 6I-J and Figure S6A). GSEA analysis showed that FA-induced MAGL-CKI mice had inhibited Wnt signaling pathway and extracellular matrix component, and activated FAO and mitochondrial biogenesis compared to FA alone group (Figure 6K-N). We also examined the levels of CB2, CB1, and Active- β -catenin in 3 groups of mice. In FAN mice, CB2 and Active- β -catenin were increased, but their upregulation was blocked by MAGL knock-in. However, CB1 levels remained unchanged after MAGL knock-in (Figure 6O-T).

Tubular cell specific MAGL knock-in mice resist lipid deposition and renal fibrosis

Subsequently, we evaluated the protein and mRNA expression levels of FAO-related genes. Consistent with the RNA-seq data, PGC-1 α , PPAR α , CPT1A, ACOX1, CPT2, and ACOX2 showed decreased expression in FAN mice, while MAGL-CKI increased their expression (Figure 7A-L). We also assessed lipid accumulation in the kidney through diverse experimental methodologies. Nile red staining and ADRP fluorescence demonstrated substantial lipid deposition in the kidneys of FAN mice, whereas MAGL-CKI ameliorated it (Figure 7M). TEM

analysis exhibited augmented lipid droplets in renal tubular cells of FAN mice, but not in MAGL-CKI mice (Figure 7N). Furthermore, the triglyceride (TG) content in kidney tissue was diminished in the MAGL-CKI group (Figure 7O). Periodic acid-schiff (PAS) and Sirius red staining demonstrated augmented tubular injury and fibrosis in FAN mice, whereas MAGL-CKI mice exhibited diminished levels of these indicators (Figure 7P-R). Likewise, fibrotic proteins such as Fibronectin and α -smooth muscle actin (α -SMA), exhibited increased expression in FAN mice, whereas a substantial decrease was displayed in MAGL-CKI group (Figure 7S-U). Additionally, we assessed the levels of inflammatory factors, confirming that MAGL transgene effectively alleviated renal inflammation (Figure S7A-D).

Supplement of recombinant MAGL effectively protects against renal fibrosis in UIRI mice

Treatment of recombinant MAGL into UIRI mice decreased albumin to creatinine ratio (ACR), Scr, and BUN levels, and reduced 2-AG levels in serum and kidney homogenates (Figure 8A-F). Immunofluorescent staining and western blot analysis demonstrated a reduction in MAGL expression in UIRI mice, concomitant with an elevation in CB2, CB1, and Active β -catenin levels. Nevertheless, the addition of MAGL effectively inhibited the upregulation of CB2 and Active β -catenin, while CB1 levels remained unaltered (Figure 8G-L). FAO-related proteins, were decreased in UIRI mice, but strongly reversed by MAGL treatment (Figure 8M-R). Nile Red staining and ADRP indicated that MAGL supplementation reduced lipid accumulation in UIRI (Figure 8R). Fibronectin, marker of fibrosis, was increased in UIRI but blocked by MAGL treatment (Figure 8S-T). PAS and Sirius Red staining revealed an increase in tubular injury and fibrosis in mice subjected to UIRI. Conversely, the administration of

MAGL supplementation retarded tubular injury and fibrosis (Figure 8U-W). Similarly, we examined the inflammatory factors levels, and confirmed that MAGL supplementation also alleviated inflammation (Figure S7E-H).

2-AG suppresses PPAR α /PGC-1 α -mediated FAO via β -catenin signaling

We then treated HK-2 cells with 2-AG. 2-AG upregulated CB2 and β -catenin but did not affect CB1 (Figure 9A-D). 2-AG was then packaged with ICG material to be visual. Of interest, we observed co-staining of 2-AG and CB2, further suggested 2-AG induced cell injury through CB2 (Figure 9E). Mitochondrial oxygen consumption rate (OCR) was measured by Seahorse analysis. Cellular OCR was determined in the basal state and upon exposure to oligomycin, p-trifluoromethoxy carbonyl cyanide phenylhydrazine (FCCP), rotenone and antimycin (Rot/AA). Etomoxir (ETO), a selective inhibitor of CPT-1, was also added to evaluate the extent of FAO. The Seahorse analysis revealed a reduction in basal and maximal OCR, as well as ATP production capacity in the cells treated with 2-AG group. Whereas, supplementation with MAGL restored these parameters (Figure 9F-I). These findings indicate that MAGL effectively restores mitochondrial FAO metabolism. In addition, 2-AG significantly reduced the protein levels of FAO-related genes in vitro (Figure 9J and Figure S8A-D). We then isolated cytosolic and nuclear proteins. 2-AG treatment induced nuclear translocation of β -catenin, the active form of β -catenin (Figure 9K-M). Immunoprecipitation analysis showed β -catenin overexpression decreased the binding of PGC-1 α and PPAR α (Figure 9N-O). Pre-treatment with the small molecule compound ICG-001 (inhibitor of β -catenin) reversed 2-AG-decreased PGC-1 α binding with PPAR α binding (Figure 9P-Q). Simultaneously, β -catenin decreased the

expression of PGC-1 α , PPAR α , and ACOX1 (Figure 9R-V). To further confirm the role of β -catenin, tubular cells were isolated from β -catenin loxp/lox mice and treated with 2-AG following the induction of β -catenin knockout (Figure S8E-G and Figure 9W). 2-AG downregulated the expression of E-cadherin, PGC-1 α , PPAR α , and CPT1A in primary cells, while inducing upregulation of β -catenin, Fibronectin, and lipid accumulation. However, these effects were effectively blocked by β -catenin knockout (Figure 9X-Y and Figure S8H-M). These findings suggest β -catenin plays a crucial role in 2-AG-induced lipid metabolism dysfunction and renal fibrosis.

Taken together, the schematic diagram demonstrates 2-AG binds to the receptor CB2 to induce β -catenin activation, and then inhibits transcriptional activity of PGC-1 α and PPAR α to block FAO-related genes expression, which results in lipid accumulation and subsequent fibrogenesis. Of note, MAGL could hydrolyze 2-AG to block the whole pathway, and then ameliorate lipid accumulation and fibrogenesis. MAGL is a promising therapeutic strategy for CKD treatments (Figure 9Z).

Discussion

CKD affects around 159 million people in China, with 26.4 million suffering from end-stage renal disease (ESRD) [39]. As to no efficacious therapies, CKD is becoming a significant public health problem worldwide. To early diagnose and effectively intervene is of utmost importance to nephrologists.

Tubular cells are responsible for absorption and secretion in kidney, and require large amounts of energy to remain active and survive [40]. Energy metabolism dysfunction in tubular

cells plays a key role in triggering CKD [41]. However, the underlying mechanisms and regulatory strategies have not been fully evaluated.

FAO is a process of fatty acid metabolism regulated by PPAR α [42,43], which controls important genes like CPT1, CPT2, ACOX1, and ACOX2 [44]. PGC-1 α enhances PPAR α activity [45]. FAO dysfunction causes fatty acid accumulation, leading to tubular injury and fibrosis [23,46]. Enhancing PPAR α activity preserves FAO function, inhibits tubular injury, and slows fibrosis [47,48]. However, further investigation is needed to identify PGC-1 α and PPAR α regulators.

ECS is an important system in the body, comprising endocannabinoids, their receptors, and regulatory enzymes. ECS is highly involved in several physiological functions, including appetite, immune regulation, pain regulation, inflammation modulation, metabolic, and also in kidney diseases [49,50]. Previous studies found CB2 triggers renal fibrosis [31,33] and may be involved in energy metabolism and lipid metabolism in renal tubular cells. However, the detailed mechanism has not been understood. Studies have shown 2-AG is a potent activator of CB2 receptor [51,52]. In UUO mice, 2-AG levels increased in kidneys [34]. However, whether 2-AG can directly cause tubular cell injury and lipid metabolism dysfunction has not been investigated.

In this study, we found serum 2-AG levels increased significantly in CKD (Figure 1). Moreover, we observed 2-AG is enriched in injured kidney of UUO. And 2-AG activated CB2/ β -catenin pathway to accelerate renal lipid accumulation and fibrosis progression (Figure 2 and Figure S1). Mechanistically, 2-AG induced CB2 and β -catenin activation, to inhibit PGC-

1 α /PPAR α -mediated FAO function (Figure 9). These results suggest 2-AG induces FAO dysfunction and lipid accumulation through CB2/ β -catenin pathway.

MAGL is an enzyme that regulates the levels of 2-AG in the body. It was initially discovered in the intestines and adipose tissues of rats and consists of an alpha/beta hydrolase fold and a catalytic triad [53]. MAGL plays a crucial role in regulating the endocannabinoid system, and blocking MAGL in the nervous system can increase 2-AG levels and activate the 2-AG signaling [54]. MAGL also indirectly affects the levels of free fatty acids and controls the levels of other lipids with pro-inflammatory or tumor-promoting effects through their hydrolysis [55]. Inhibition of MAGL has been shown to enhance 2-AG-mediated CB2 signaling and ameliorate injury and inflammation caused by hepatic ischemia-reperfusion [56]. MAGL inhibition can exacerbate acute myocardial infarction in mice by mobilizing myeloid cells through 2-AG [57]. Increased MAGL expression promotes cancer cell invasion and tumor growth by regulating free fatty acid levels in human cancers [58]. Besides regulating ECS, MAGL is also involved in various other processes such as lipid catabolism, energy metabolism, and activation of lipid-related signal transduction pathways [36,59]. However, the role of MAGL in kidney diseases has not been well understood.

Interestingly, we observed a decrease in MAGL expression in kidneys of both multiple mice models and clinical patients (Figure 3). We also ascertained the possibility of MAGL being the potential prognostic factor in CKD (Figure 4). We therefore speculated that MAGL can be applied as a strategy to prevent and treat 2-AG-induced fibrosis. The role of MAGL was comprehensively assessed by genetic and pharmacological approaches in CKD models. The

efficacies of MAGL to improve renal function and ameliorate kidney fibrosis were confirmed by studies in transgenic mice, exogenous application of recombinant protein (Figure 5-8). In contrast to its promoting role of MAGL in liver injury, our findings for the first time indicate MAGL protects against lipotoxicity and inflammation in renal fibrosis (Figures 5-8, S7). This implies that MAGL may exert distinct effects in the liver and kidneys, possibly due to tissue-specific and cell-specific actions.

Our new findings show MAGL, besides serving as a monoacylglycerol lipase involving direct lipid hydrolysis, innovatively exhibits special roles in FAO metabolism related to 2-AG/CB2 signaling. This dual functionality effectively alleviates lipotoxicity in renal tubular cells. Consequently, MAGL emerges as a promising candidate for mitigating tubular cell damage and renal fibrosis. Large quantities of researches have confirmed the substantial accumulation of triglycerides and saturated free fatty acids in CKD, both of which contribute to organelle structural damage, oxidative stress, inflammatory responses, and cell death. Various pharmacological interventions, such as lipid-lowering drugs of fluvastatin [60], PPAR α agonist fenofibrate [61], and the sodium-glucose cotransporter 2 (SGLT2) inhibitor canagliflozin [62], could greatly attenuate lipid-induced kidney injury and fibrosis. In contrast, MAGL, being an endogenously well-expressed component in the kidneys, presents a significant advantage compared to those small compounds. Replenishing MAGL during renal injury demonstrates its dual efficiencies in lipid hydrolysis and FAO, making it a promising avenue for further investigation and therapeutic intervention study.

β -catenin is normally silent in adult kidneys but becomes reactivated in CKD and renal

fibrosis [63]. β -catenin could induce multiple targets to trigger tubular cell injury [64–66]. We found β -catenin not only mediates CB2-induced renal tubular injury but also inhibits PGC-1 α [29,33], an important regulator for FAO function. To investigate if β -catenin mediates 2-AG-induced lipid metabolism dysfunction, we isolated primary cultured tubular cells from β -catenin-knockout and used inhibitor methods to find that β -catenin suppresses PGC-1 α and PPAR α and impedes their interaction, ultimately leading to impaired FAO function (Figure 9).

Therefore, we innovatively discovered that MAGL, through hydrolyzing 2-AG, effectively restores FAO by suppressing 2-AG/ β -catenin signaling, thereby alleviating lipotoxicity in tubular cells and mitigating renal fibrosis. Our study revealed a novel mechanism underlying lipid accumulation in renal tubular cells during CKD. Importantly, our findings propose that MAGL not only holds promise as a diagnostic indicator for renal function decline but also emerges as a new therapeutic target for CKD.

Concise methods

For detailed methods, see the Supplementary Methods.

Human clinical specimens

Human specimens (urine, serum, and kidney biopsies) were collected from CKD patients at the First People's Hospital of Foshan. Normal control biopsies were obtained from paracancerous tissues of patients undergoing nephrectomy. Demographic and clinical data are presented in Supplementary Table S1 - S3. Studies involving human samples were approved by the Medical Ethics Committee of the First People's Hospital of Foshan (FSYYY – EC – SOP – 008 - 02.0 - A09) and performed with informed patient consent.

MAGL enzyme-linked immunosorbent assay

We used an ELISA kit to measure urinary MAGL concentration and corrected it by urine creatinine.

Animal models

Male C57BL/6 mice were purchased from the Experimental Animal Center of Southern Medical University. Tubule-specific MAGL conditional knock-in mice were purchased from Cyagen Biosciences.

We used different methods to induce various kidney disease models in mice: unilateral ureteral obstruction (UUO) by double-ligation of the left ureter, folic acid-induced nephropathy by intraperitoneal injection, unilateral ischemia reperfusion injury (UIRI) by renal pedicle clipping.

Animal studies were performed according to the Guidelines for the Care and Use of Laboratory Animals and approved by the Animal Ethics Committee at Nanfang Hospital, Southern Medical University (NFYY – 2020 - 0837).

Generation of β -catenin loxp/loxp mice

C57BL/6 β -catenin loxp/loxp mice were generated by CRISPR/Cas9 system.

Tubule-specific MAGL conditional knock-in mice and genotyping

The construction of MAGL-CKI was achieved by applying CRISPR/Cas9 for the knock-in of MAGL gene into Rosa26 of C57BL/6 zygotes.

Urinary albumin, serum creatinine and BUN assay

Urinary albumin was measured using a mouse Albumin ELISA Quantitation kit, and

standardized to urine creatinine. Serum creatinine and BUN levels were determined by an automatic chemistry analyzer.

Preparation of 2-AG Nanoparticles

We prepared liposomes containing DPPC: DSPE-PEG2000 in a 95 : 5 molar ratio using the thin film hydration method⁵³. Lipid and 2-AG in a weight ratio of 20 : 1 were dissolved in 30 ml CHCl₃ and evaporated at 25 °C to form a thin lipid film. Residual solvent was removed in vacuum for 6 h. ICG in a PBS solution (500 µg/mL) was added to the lipid film and encapsulated by rotary evaporation at 25 °C. The crude liposome was extruded 11 times through a 100 nm filter using an Avanti Polar Lipids mini-extruder.

***In vivo* Bioimaging of 2-AG distribution**

After Sham or UUO surgery, C57BL/6 mice were intravenously injected with 2-AG-loaded nanoparticles at 10 mg/kg body weight, 3 d after surgery under general anesthesia. 2 h later, fluorescence images were visualized using a Bruker FX PRO imaging system with excitation at 785 nm and emission at 810 nm. All procedures were conducted in the dark.

LC-MS

To prepare plasma, cell, or kidney tissue samples, we added 200 µl of toluene to 200 µl of plasma, 10⁷ cells, or 20 mg of kidney tissue. After grinding, crushing, and centrifuging at 13,000 rpm at 4 °C for 10 min, we transferred the upper organic phase to a 1.5 ml EP tube and dried it using a nitrogen blower. The residue was then resolved by adding 100 µl of 75% methanol and shaking for 30 s. LC-MS analysis was performed after centrifuging at 14,000 rpm at 4 °C for 20 min. We used LC-MS grade solvents and the following standard reagents: 2-AG

426 and AEA.

427 **Transmission Electron Microscopy**

428 Kidney cortex was fixed in 1.25% glutaraldehyde/0.1 M phosphate buffer. Ultrathin sections
429 (60 nm) were prepared by a routine procedure and examined under an electron microscope.

430 **Western blot analysis and immunoprecipitation**

431 Protein expression was analyzed by western blot analysis. The interaction among proteins
432 was detected by coimmunoprecipitation [67]. Primary antibodies used were described in the
433 Supplementary Methods.

434 **Reverse transcription and real-time PCR**

435 RNA was isolated using TRIzol RNA isolation system, and real-time PCR was performed on
436 an ABI PRISM 7000 Sequence Detection System. The primer sequences are listed in
437 Supplementary Table S4.

438 **Cell Culture and Treatment**

439 Human proximal tubular cell line (HK-2) was purchased from the Cell Bank of the Chinese
440 Academy of Sciences. Nuclear and cytoplasmic fractions were separated with a commercial kit.
441 ATP production was determined using enhanced ATP assay kit.

442 **Seahorse assay**

443 HK-2 cells were treated with 2-AG alone or in combination with MAGL, and their metabolic
444 profiles were assessed using a Seahorse XF96 Analyzer. OCR was measured, and mitochondrial
445 function and FAO were evaluated through specific injections.

Isolation of tubular epithelial cells and treatment

We isolated and cultured primary mouse kidney tubular cells from β -catenin loxp/loxp mice or MAGL-CKI mice following a routine protocol, which involved mincing the kidneys and digesting them with collagenase. After growing the cells for 4-8 d, the cells isolated from β -catenin loxp/loxp mice were transfected with Adv-CMV-Cre and then treated with 100 μ M 2-AG for 24 h. The primary renal tubular epithelial cells isolated from MAGL-CKI mice were treated with TGF- β 1 (5 ng/ml) for 24 h. We then harvested the cells for analysis.

Histology, immunohistochemical and immunofluorescence staining

Paraffin-embedded kidney sections were performed with Periodic Acid-Schiff (PAS) and Sirius red staining to identify injured tubules and collagen deposition. Nile red staining, immunohistochemical and immunofluorescence staining were performed using routine protocols. Antibodies are described in the Supplementary Methods.

Transcriptomic analysis

RNA-seq was performed on kidney tissues from different groups of mice using TRIzol reagent and Illumina Novaseq platform. Gene expression was quantified, and differential expression analysis was conducted with DESeq2. Pathway enrichment analysis was performed using clusterProfiler and Reactome, while GSEA analysis was conducted using various databases.

Untargeted Metabolomics

Tissue samples were collected and prepared according to the manufacturer's instructions. UHPLC-MS/MS analyses were completed by an UHPLC (ThermoFisher, Germany) coupled

with an Orbitrap Q ExactiveTM HF mass spectrometer (Thermo Fisher, Germany) in Novogene Co., Ltd. (Beijing, China). The raw data were processed by the Compound Discoverer 3.3 (CD3.3, ThermoFisher), including peak alignment, peak picking, and metabolite identification. Pareto-scaled principal component analysis (PCA) and orthogonal partial least-squares discriminant analysis (OPLS - DA) were performed at meta X. The metabolites with Variable Importance in the Projection (VIP) > 1 and *P*-value < 0.05 were assigned as significant changed.

Statistical analyses

Data were presented as mean with SEM, and statistical analysis was performed using IBM SPSS Statistics 25. We used Chi-square test for comparing two rates or two composition ratios. For the parametric analysis, we used Student's t-test for comparing two groups and one-way ANOVA followed by the Least Significant Difference or Dunnett's T3 procedure for comparing more than two groups. A *P*-value < 0.05 was considered significant. Bivariate correlation analysis was conducted using Pearson and Spearman rank correlation analysis.

Data availability

Transcriptomics data in this study has been uploaded to the NCBI SRA database (accession number: PRJNA987376, PRJNA974908). The metabolomics data in this study are available in the MetaboLights database (MTBLS9333). The authors are willing to provide other raw data that support the findings of this article to qualified researchers without any hesitation.

Acknowledgments

This work was supported by National Natural Science Foundation of China Grant 82225010, 82070707, 82000652, 82100786; National Key R&D Program of China (2020YFC2005000);

and Outstanding Youths Development Scheme of Nanfang Hospital, Southern Medical University (2019J013, 2021J001); and a Postdoctoral Science Foundation of China grant (2021M701636).

Conflict of interests

The authors have no conflict of interests in this paper.

Authors' contributions

Shan Zhou, Xian Ling, Jielin Zhu, Ye Liang, Qijian Feng, Chao Xie, Jiemei Li, Qiyang Chen, Shuangqin Chen, Jinhua Miao, Mengyao Zhang, Zhiru Li, Weiwei Shen, Xiaolong Li, Qinyu Wu, Xiaoxu Wang, Ruiyuan Liu, Cheng Wang, Fan Fan Hou, Yaozhong Kong, Youhua Liu and Lili Zhou performed the experiments and contributed to acquisition and analysis of the data. Lili Zhou, Youhua Liu and Yaozhong Kong conceived the research and designed the experiments. Qiyang Chen and Chao Xie provided patients' samples and clinical information. Shan Zhou, Xian Ling, Jielin Zhu, Ye Liang, Qijian Feng and Chao Xie created the figures and prepared the materials of this study. Shan Zhou, Xian Ling, Jielin Zhu, Ye Liang and Lili Zhou wrote the manuscript. All authors contributed to the article and approved the final manuscript.

References

1. Chen TK, Knicely DH, Grams ME. Chronic Kidney Disease Diagnosis and Management: A Review. JAMA. 2019; 322: 1294–1304.
2. Ruiz-Ortega M, Rayego-Mateos S, Lamas S, Ortiz A, Rodrigues-Diez RR. Targeting the

- progression of chronic kidney disease. *Nat Rev Nephrol.* 2020; 16: 269–288.
3. Lan HY, Nikolic-Paterson DJ. Editorial: Advances in Mechanisms of Renal Fibrosis. *Front Physiol.* 2018; 9: 284.
4. Yuan Q, Ren Q, Li L, Tan H, Lu M, Tian Y, et al. A Klotho-derived peptide protects against kidney fibrosis by targeting TGF- β signaling. *Nat Commun.* 2022; 13: 438.
5. Djudjaj S, Boor P. Cellular and molecular mechanisms of kidney fibrosis. *Mol Aspects Med.* 2019; 65: 16–36.
6. Qi R, Yang C. Renal tubular epithelial cells: the neglected mediator of tubulointerstitial fibrosis after injury. *Cell Death Dis.* 2018; 9: 1126.
7. Gewin LS. Renal fibrosis: Primacy of the proximal tubule. *Matrix Biol.* 2018; 68-69: 248-262.
8. Marchese E, Caterino M, Viggiano D, Cevenini A, Tolone S, et al. Metabolomic fingerprinting of renal disease progression in Bardet-Biedl syndrome reveals mitochondrial dysfunction in kidney tubular cells. *iScience.* 2022; 25: 105230.
9. Piret SE, Mallipattu SK. Transcriptional regulation of proximal tubular metabolism in acute kidney injury. *Pediatr Nephrol.* 2023; 38: 975–986.
10. Knottnerus SJG, Bleeker JC, Wüst RCI, Ferdinandusse S, IJlst L, Wijburg FA, et al. Disorders of mitochondrial long-chain fatty acid oxidation and the carnitine shuttle. *Rev Endocr Metab Disord.* 2018; 19: 93–106.
11. Guerra IMS, Ferreira HB, Melo T, Rocha H, Moreira S, Diogo L, et al. Mitochondrial Fatty Acid β -Oxidation Disorders: From Disease to Lipidomic Studies-A Critical Review. *Int J Mol Sci.* 2022; 23: 13933.
12. Kalim S, Rhee EP. An overview of renal metabolomics. *Kidney Int.* 2017; 91: 61–69.
13. Zhu Z, Hu J, Chen Z, Feng J, Yang X, Liang W, et al. Transition of acute kidney injury to chronic kidney disease: role of metabolic reprogramming. *Metabolism.* 2022; 131: 155194.
14. Chen FJ, Yin Y, Chua BT, Li P. CIDE family proteins control lipid homeostasis and the development of metabolic diseases. *Traffic.* 2020; 21: 94–105.
15. Mota M, Banini BA, Cazanave SC, Sanyal AJ. Molecular mechanisms of lipotoxicity and glucotoxicity in nonalcoholic fatty liver disease. *Metabolism.* 2016; 65: 1049–1061.
16. Zhang Y, Ma KL, Ruan XZ, Liu BC. Dysregulation of the Low-Density Lipoprotein

- Receptor Pathway Is Involved in Lipid Disorder-Mediated Organ Injury. *Int J Biol Sci.* 2016; 12: 569–579.
17. Wang Y, Ran L, Lan Q, Liao W, Wang L, Wang Y, et al. Imbalanced lipid homeostasis caused by membrane α Klotho deficiency contributes to the acute kidney injury to chronic kidney disease transition. *Kidney Int.* 2023; 104: 956–974.
18. Zhang Y, Yao H, Li C, Sun W, Chen X, Cao Y, et al. Gandi Capsule Improved Podocyte Lipid Metabolism of Diabetic Nephropathy Mice through SIRT1/AMPK/HNF4A Pathway. *Oxid Med Cell Longev.* 2022; 2022: 6275505.
19. Jin L, Ye H, Pan M, Chen Y, Ye B, Zheng Y, et al. Kruppel-like factor 4 improves obesity-related nephropathy through increasing mitochondrial biogenesis and activities. *J Cell Mol Med.* 2020; 24: 1200–1207.
20. Figueroa-Juárez E, Noriega LG, Pérez-Monter C, Alemán G, Hernández-Pando R, Correa-Rotter R, et al. The Role of the Unfolded Protein Response on Renal Lipogenesis in C57BL/6 Mice. *Biomolecules.* 2021; 11: 73.
21. Wahl P, Ducasa GM, Fornoni A. Systemic and renal lipids in kidney disease development and progression. *Am J Physiol Renal Physiol.* 2016; 310: F433-445.
22. Herman-Edelstein M, Scherzer P, Tobar A, Levi M, Gafter U. Altered renal lipid metabolism and renal lipid accumulation in human diabetic nephropathy. *J Lipid Res.* 2014; 55: 561–572.
23. Kang HM, Ahn SH, Choi PS, Ko YA, Han SH, Chinga F, et al. Defective fatty acid oxidation in renal tubular epithelial cells has a key role in kidney fibrosis development. *Nat Med.* 2015; 21: 37–46.
24. Liu L, Ning X, Wei L, Zhou Y, Zhao L, Ma F, et al. Twist1 downregulation of PGC-1 α decreases fatty acid oxidation in tubular epithelial cells, leading to kidney fibrosis. *Theranostics.* 2022; 12: 3758-3775.
25. Li J, Yang Y, Li Q, Wei S, Zhou Y, Yu W, et al. STAT6 contributes to renal fibrosis by modulating PPAR α -mediated tubular fatty acid oxidation. *Cell Death Dis.* 2022; 13: 66.
26. Jang HS, Noh MR, Kim J, Padanilam BJ. Defective Mitochondrial Fatty Acid Oxidation and Lipotoxicity in Kidney Diseases. *Front Med (Lausanne).* 2020; 7: 65.
27. Han SH, Wu MY, Nam BY, Park JT, Yoo TH, Kang SW, et al. PGC-1 α Protects from Notch-Induced Kidney Fibrosis Development. *J Am Soc Nephrol.* 2017; 28: 3312-3322.
28. Gai Z, Wang T, Visentin M, Kullak-Ublick GA, Fu X, Wang Z. Lipid Accumulation and Chronic Kidney Disease. *Nutrients.* 2019; 11: 722.

29. Miao J, Liu J, Niu J, Zhang Y, Shen W, Luo C, et al. Wnt/ β -catenin/RAS signaling mediates age-related renal fibrosis and is associated with mitochondrial dysfunction. *Aging Cell*. 2019; 18: e13004.
30. Lu HC, Mackie K. Review of the endocannabinoid system. *Biol Psychiatry Cogn Neurosci Neuroimaging*. 2021; 6: 607–615.
31. Zhou S, Wu Q, Lin X, Ling X, Miao J, Liu X, et al. Cannabinoid receptor type 2 promotes kidney fibrosis through orchestrating β -catenin signaling. *Kidney Int*. 2020; 99: 364–381.
32. Zhou L, Zhou S, Yang P, Tian Y, Feng Z, Xie XQ, et al. Targeted inhibition of the type 2 cannabinoid receptor is a novel approach to reduce renal fibrosis. *Kidney Int*. 2018; 94: 756–772.
33. Zhou S, Ling X, Meng P, Liang Y, Shen K, Wu Q, et al. Cannabinoid receptor 2 plays a central role in renal tubular mitochondrial dysfunction and kidney ageing. *J Cell Mol Med*. 2021; 25: 8957–8972.
34. Lecru L, Desterke C, Grassin-Delyle S, Chatziantoniou C, Vandermeersch S, Devocelle A, et al. Cannabinoid receptor 1 is a major mediator of renal fibrosis. *Kidney Int*. 2015; 88: 72–84.
35. Dinh TP, Carpenter D, Leslie FM, Freund TF, Katona I, Sensi SL, et al. Brain monoglyceride lipase participating in endocannabinoid inactivation. *Proc Natl Acad Sci U S A*. 2002; 99: 10819–10824.
36. Omran Z. New Disulfiram Derivatives as MAGL-Selective Inhibitors. *Molecules*. 2021; 26: 3296.
37. Xiang W, Shi R, Kang X, Zhang X, Chen P, Zhang L, et al. Monoacylglycerol lipase regulates cannabinoid receptor 2-dependent macrophage activation and cancer progression. *Nat Commun*. 2018; 9: 2574.
38. Heid HW, Moll R, Schwetlick I, Rackwitz HR, Keenan TW. Adipophilin is a specific marker of lipid accumulation in diverse cell types and diseases. *Cell Tissue Res*. 1998; 294: 309–321.
39. Liyanage T, Toyama T, Hockham C, Ninomiya T, Perkovic V, Woodward M, et al. Prevalence of chronic kidney disease in Asia: a systematic review and analysis. *BMJ Glob Health*. 2022; 7: e007525.
40. Wang K, Kestenbaum B. Proximal tubular secretory clearance: a neglected partner of kidney function. *Clin J Am Soc Nephrol*. 2018; 13: 1291–1296.

41. Fontecha-Barriuso M, Lopez-Diaz AM, Guerrero-Mauvecin J, Miguel V, Ramos AM, Sanchez-Niño MD, et al. Tubular mitochondrial dysfunction, oxidative stress, and progression of chronic kidney disease. *Antioxidants (Basel)*. 2022; 11: 1356.
42. Piret SE, Attallah AA, Gu X, Guo Y, Gujarati NA, Henein J, et al. Loss of proximal tubular transcription factor Krüppel-like factor 15 exacerbates kidney injury through loss of fatty acid oxidation. *Kidney Int*. 2021; 100: 1250–1267.
43. Du M, Wang X, Yuan L, Liu B, Mao X, Huang D, et al. Targeting NFATc4 attenuates non-alcoholic steatohepatitis in mice. *J Hepatol*. 2020; 73: 1333–1346.
44. Tran NKS, Kim GT, Park SH, Lee D, Shim SM, Park TS. Fermented *Cordyceps militaris* Extract Prevents Hepatosteatosis and Adipocyte Hypertrophy in High Fat Diet-Fed Mice. *Nutrients*. 2019; 11: 1015.
45. Zhang C, Huang Z, Jing H, Fu W, Yuan M, Xia W, et al. SAK-HV Triggered a Short-period Lipid-lowering Biotherapy Based on the Energy Model of Liver Proliferation via a Novel Pathway. *Theranostics*. 2017; 7: 1749-1769.
46. Su H, Wan C, Lei CT, Zhang CY, Ye C, Tang H, et al. Lipid Deposition in Kidney Diseases: Interplay Among Redox, Lipid Mediators, and Renal Impairment. *Antioxid Redox Signal*. 2018; 28: 1027-1043.
47. Chung KW, Lee EK, Lee MK, Oh GT, Yu BP, Chung HY. Impairment of PPAR α and the Fatty Acid Oxidation Pathway Aggravates Renal Fibrosis during Aging. *J Am Soc Nephrol*. 2018; 29: 1223–1237.
48. Liu F, Zhuang S. New Therapies for the Treatment of Renal Fibrosis. *Adv Exp Med Biol*. 2019; 1165: 625–659.
49. Gonçalves ECD, Baldasso GM, Bicca MA, Paes RS, Capasso R, Dutra RC. Terpenoids, Cannabimimetic Ligands, beyond the Cannabis Plant. *Molecules*. 2020; 25: 1567.
50. Chua JT, Argueta DA, DiPatrizio NV, Kovesdy CP, Vaziri ND, Kalantar-Zadeh K, et al. Endocannabinoid System and the Kidneys: From Renal Physiology to Injury and Disease. *Cannabis Cannabinoid Res*. 2019; 4: 10–20.
51. Silveira KM, Wegener G, Joca SRL. Targeting 2-arachidonoylglycerol signalling in the neurobiology and treatment of depression. *Basic Clin Pharmacol Toxicol*. 2021; 129: 3–14.
52. Ten-Blanco M, Flores Á, Pereda-Pérez I, Piscitelli F, Izquierdo-Luengo C, Cristino L, et al. Amygdalar CB2 cannabinoid receptor mediates fear extinction deficits promoted by orexin-A/hypocretin-1. *Biomed Pharmacother*. 2022; 149: 112925.

53. Karlsson M, Contreras JA, Hellman U, Tornqvist H, Holm C. cDNA cloning, tissue distribution, and identification of the catalytic triad of monoglyceride lipase. *J Biol Chem.* 1997; 272: 27218–27223.
54. Serrano A, Pavon FJ, Buczynski MW, Schlosburg J, Natividad LA, Polis IY, et al. Deficient endocannabinoid signaling in the central amygdala contributes to alcohol dependence-related anxiety-like behavior and excessive alcohol intake. *Neuropsychopharmacology.* 2018; 43: 1840–1850.
55. Kienzl M, Hasenoechl C, Maitz K, Sarsembayeva A, Taschler U, Valadez-Cosmes P, et al. Monoacylglycerol lipase deficiency in the tumor microenvironment slows tumor growth in non-small cell lung cancer. *OncoImmunology.* 2021; 10: 1965319–1965319.
56. Cao Z, Mulvihill MM, Mukhopadhyay P, Xu H, Erdélyi K, Hao E, et al. Monoacylglycerol lipase controls endocannabinoid and eicosanoid signaling and hepatic injury in mice. *Gastroenterology.* 2013; 144: 808-817.e15.
57. Schloss MJ, Horekmans M, Guillamat-Prats R, Hering D, Lauer E, Lenglet S, et al. 2-Arachidonoylglycerol mobilizes myeloid cells and worsens heart function after acute myocardial infarction. *Cardiovasc Res.* 2019; 115: 602–613.
58. Nomura DK, Long JZ, Niessen S, Hoover HS, Ng S-W, Cravatt BF. Monoacylglycerol lipase regulates a fatty acid network that promotes cancer pathogenesis. *Cell.* 2010; 140: 49–61.
59. Papa A, Pasquini S, Contri C, Gemma S, Campiani G, Butini S, et al. Polypharmacological Approaches for CNS Diseases: Focus on Endocannabinoid Degradation Inhibition. *Cells.* 2022; 11: 471.
60. Gheith OA, Sobh MA-K, Mohamed KE-S, El-Baz MA, El-Husseini F, Gazarin SS, et al. Impact of treatment of dyslipidemia on renal function, fat deposits and scarring in patients with persistent nephrotic syndrome. *Nephron.* 2002; 91: 612–619.
61. Tanaka Y, Kume S, Araki S, Isshiki K, Chin-Kanasaki M, Sakaguchi M, et al. Fenofibrate, a PPAR α agonist, has renoprotective effects in mice by enhancing renal lipolysis. *Kidney Int.* 2011; 79: 871–882.
62. Yang Y, Li Q, Ling Y, Leng L, Ma Y, Xue L, et al. m6A eraser FTO modulates autophagy by targeting SQSTM1/P62 in the prevention of canagliflozin against renal fibrosis. *Front Immunol.* 2023; 13: 1094556.
63. Zhou L, Chen X, Lu M, Wu Q, Yuan Q, Hu C, et al. Wnt/ β -catenin links oxidative stress to podocyte injury and proteinuria. *Kidney Int.* 2019; 95: 830–845.

731 64. Tan RJ, Zhou D, Zhou L, Liu Y. Wnt/ β -catenin signaling and kidney fibrosis. *Kidney Int*
732 *Suppl* (2011). 2014; 4: 84–90.

733
734 65. Zhou L, Liu Y. Wnt/ β -catenin signaling and renin-angiotensin system in chronic kidney
735 disease. *Curr Opin Nephrol Hypertens*. 2016; 25: 100–106.

736
737 66. Zhou D, Tian Y, Sun L, Zhou L, Xiao L, Tan RJ, et al. Matrix Metalloproteinase-7 Is a
738 Urinary Biomarker and Pathogenic Mediator of Kidney Fibrosis. *J Am Soc Nephrol*. 2017; 28:
739 598-611.

740
741 67. Li J, Niu J, Min W, Ai J, Lin X, Miao J, et, al. B7-1 mediates podocyte injury and
742 glomerulosclerosis through communication with Hsp90ab1-LRP5- β -catenin pathway. *Cell*
743 *Death Differ*. 2022; 29: 2399-2416.

Figure legends

Figure 1. 2-AG increases in CKD and drives lipid deposition and fibrogenesis in tubular cells

A. Representative graphs showing 2-AG levels in serum from healthy people and CKD patients at stage 5. 2-AG were identified by liquid chromatograph mass spectrometry (LC/MS) analysis.

B. Table showing the detectable rate of 2-AG in serum from healthy people and CKD patients at stage 5. C. Representative graph showing 2-AG levels in serum from healthy people and CKD patients at stage 5 by LC/MS analysis. $**P < 0.01$ versus the healthy control group. $n = 34$ (healthy control); $n = 44$ (CKD patients at 5 stage). D-E. Representative graphs showing 2-AG levels in serum and kidney homogenates by LC/MS analysis. UUO mice were sacrificed at 7 d after surgery. $*P < 0.05$, $**P < 0.01$ versus the sham control group alone. $n = 5$. F. Representative graph showing 2-AG levels in serum of FA and sham group of mice, which were identified by LC/MS analysis. $*P < 0.05$ versus the sham control group alone. $n = 5$. FA: folic acid. G. HK-2 cells were treated with 2-AG (100 μ M) for 24 h. H. Representative graph showing ATP levels in 2 groups. $***P < 0.001$ versus the control group. $n = 6$. I. Representative immunofluorescence micrographs showing the expression of lipid (Nile Red staining) in 2 groups. White arrow indicates positive staining. Scale bar, 25 μ m. J-L. Representative western blot and quantitative data showing the expression of Fibronectin and Vimentin in 2 groups. Numbers (1–3) indicate each individual culture in a given group. $**P < 0.01$, $***P < 0.001$ versus the control group alone. $n = 3$. M. Representative immunofluorescence micrographs showing the expression of Fibronectin in 2 groups. White arrow indicates positive staining.

Scale bar, 50 μ m.

Figure2. 2-AG accelerates lipid deposition and renal fibrosis in UUO mice

A. Experimental design. Mice were performed UUO or sham surgery. Red bar indicates intravenous injections of 2-AG (10 mg/kg/d) or vehicle for 7 d. Mice were sacrificed at 10 d after surgery. **B.** *In vivo* fluorescence image showing 2-AG was enriched in UUO-affected kidney. 2-AG (10 mg/kg) was first labeled with ICG and was injected into UUO or sham mice through tail vein for 2 h. Images were taken from UUO or sham animals by a Bruker Small Animal Optical Imaging System. **C.** Representative micrographs showing the localization of ICG-labeled 2-AG in UUO mice. White arrow indicates positive staining. Scale bar, 50 μ m. **D.** Representative graph showing 2-AG levels in kidney homogenates by LC/MS analysis. *** $P < 0.001$ versus the sham control group alone; $^{\varphi\varphi\varphi}P < 0.001$ versus the 2-AG group alone; $^{\dagger\dagger\dagger}P < 0.001$ versus the UUO group alone. $n = 5$. **E.** Representative heatmap plot of transcriptomic analysis showing the changes in Extracellular matrix, Fatty acid metabolism, Lipid metabolism and Mitochondria-related gene in 2 groups. Numbers (1 – 3) indicate each individual animal in a given group. **F.** Representative micrographs showing colocalization of 2-AG and segment-specific tubular markers in UUO/2-AG mice. Kidney sections were stained for various segment-specific tubular markers (red) by immunofluorescence. The following segment-specific tubular markers were used: proximal tubule, Aquaporin-1 (AQP1); distal tubule, sodium-chloride cotransporter (NCC); and collecting duct, Aquaporin-3 (AQP3). 2-AG was detected by the fluorescence of ICG. White arrows indicate positive tubules with colocalization of 2-AG and specific tubular markers. Scale bar, 50 μ m. **G.** Representative western blot showing renal CB2 and Active- β -catenin expressions in different groups. Numbers (1 – 2)

indicate each individual animal in a given group. n = 5. **H.** Representative micrographs showing the expression of CB2 (top) and Active- β -catenin (bottom) in 4 groups. White arrows indicate positive staining. Scale bar, 50 μ m. **I.** Representative micrographs showing colocalization of β -catenin (red) and 2-AG (green) in UUO/2-AG mice. White arrow indicates positive tubules with colocalization of 2-AG and β -catenin. Scale bar, 25 μ m. **J.** Representative transmission electron microscopy (TEM) images showing the lipid droplets in renal tubular epithelial cells in 4 groups. Yellow arrows indicate lipid droplets. Scale bar, 1 μ m. **K.** Representative western blot showing renal expression of PGC-1 α , PPAR α , CPT1A, ACOX1, Fibronectin, Collagen I and Vimentin in different groups. Numbers (1 – 2) indicate each individual animal in a given group. n = 5. **L.** Representative micrographs showing the expression of lipid droplets (Nile Red staining), ADRP, PPAR α , CPT1A and Fibronectin in 4 groups. Arrows indicate positive staining. For Nile Red and PPAR α staining, scale bar, 25 μ m; for ADRP, CPT1A and Fibronectin staining, scale bar, 50 μ m.

Figure 3. MAGL is decreased in CKD and correlated with preservation of kidney function

A. Schematic diagram showing MAGL hydrolyzing 2-AG. The ester bond at the sn-2 position of 2-AG was broken by MAGL to form arachidonic acid (AA) and glycerol. **B.** Representative micrographs showing colocalization of MAGL and various segment-specific tubular markers in kidneys from healthy control. Kidney sections were stained for MAGL (red) and various segment-specific tubular markers (green) by immunofluorescence. The following segment-specific tubular markers were used: proximal tubule, lotus tetragonolobus lectin (LTL); distal tubule, peanut agglutinin (PNA); and collecting duct, dolichos biflorus agglutinin (DBA). White arrows indicate positive tubules with colocalization of MAGL and specific tubular

830 markers. Scale bar, 50 μ m. **C.** Representative immunofluorescence micrographs showing the
831 expression of MAGL in healthy control and CKD patients at different stages. White arrow
832 indicates positive staining. Scale bar, 50 μ m. **D.** Quantitative data showing quantification of
833 MAGL positive staining in healthy control and CKD patients at different stages. n = 15 (healthy
834 control); n = 34 (patients at CKD stage 1); n = 23 (patients at CKD stage 2); n = 18 (patients at
835 CKD stage 3); n = 14 (patients at CKD stage 4-5). *** $P < 0.001$ versus healthy control group
836 alone; # $P < 0.05$ versus CKD stage 1 patient group; † $P < 0.05$ versus CKD stage 2 patients
837 group. **E.** Quantitative data showing urinary MAGL in healthy control and CKD patients at
838 different stages. n = 13 (healthy control); n = 54 (patients at CKD stage 1-2); n = 32 (patients
839 at CKD stage 3-4); n = 22 (patients at CKD stage 5). * $P < 0.05$ versus healthy control group;
840 ## $P < 0.01$, ### $P < 0.001$ versus CKD stage 1 - 2 patient group. **F.** Linear regression showing the
841 Spearman correlation coefficient (R_s) and P value between positive staining levels of renal
842 MAGL and eGFR from CKD patients respectively. n = 89. **G.** Linear regression showing the
843 Spearman correlation coefficient (R_s) and P value between urinary MAGL and eGFR from
844 CKD patients respectively. n = 108. **H.** Representative micrographs showing renal expression
845 of MAGL in healthy control and CKD patients with different etiologies, such as Focal
846 Segmental Glomerulosclerosis (FSGS), Diabetic Kidney Disease (DKD) and Lupus Nephritis.
847 Arrow indicates positive staining. Scale bar, 50 μ m. **I.** Quantitative data showing the mRNA
848 level of MAGL in mice with or without intraperitoneal injection of folic acid at 250 mg/kg.
849 Mice were sacrificed at 14 d after injection. *** $P < 0.001$ versus the sham control group alone.
850 n = 5. **J.** Quantitative data showing the mRNA level of MAGL in UUO and sham mice. UUO
851 mice were sacrificed at 7 d after surgery. *** $P < 0.001$ versus the sham control group alone. n

= 5. **K.** Representative immunofluorescence micrographs showing renal MAGL expression in different groups. Mice were sacrificed at different days after UUO surgery. White arrow indicates positive staining. Scale bar, 50 μ m. **L.** Representative western blot showing the expression of MAGL in different groups. Numbers (1 – 3) indicate each individual animal in a given group. n = 5.

Figure 4. Loss of MAGL correlates with lipid accumulation and fibrosis

A. Representative micrographs showing co-staining of MAGL and CB2, MAGL and Active- β -catenin, MAGL and ADRP, and MAGL and Fibronectin in kidneys from sham and UUO mice. Kidney sections were stained for CB2, Active- β -catenin, ADRP, Fibronectin (red) and MAGL (green) by immunofluorescence. Arrows indicate positive staining. Scale bar, 50 μ m. **B.** Representative western blot showing the expression of MAGL, CPT1A and Active- β -catenin in UUO and sham mice. Numbers (1 – 5) indicate each individual animal in a given group. n = 5. **C.** Representative micrographs showing renal MAGL (left) and β -catenin (right) expression in healthy control and CKD patient. Black arrows indicate positive staining. Scale bar, 50 μ m. **D.** Linear regression showing the Spearman correlation coefficient (R_s) and P value between positive staining level of MAGL and β -catenin from CKD patients respectively. n = 89. **E.** Representative micrographs showing renal MAGL (left) and CPT1A (right) expression in sequential sections from healthy control and CKD patient. Black arrows indicate positive staining. Scale bar, 50 μ m. **F.** Representative micrographs showing co-staining of MAGL and ADRP in kidneys from healthy control and CKD patient. Kidney sections were stained for MAGL (green) and ADRP (red) by immunofluorescence. Arrows indicate positive staining. Scale bar, 25 μ m. **G.** Linear regression showing the Spearman correlation coefficient (R_s) and

P value between positive staining levels of MAGL and ADRP from CKD patients respectively.
n = 89. **H-I.** Linear regression showing the Spearman correlation coefficient (*R_s*) and *P* value
between positive staining levels of MAGL and injury tubules or fibrotic area from CKD patients
respectively. n = 89. **J.** Representative micrographs showing co-staining of MAGL and
Fibronectin in kidneys from healthy control and CKD patient. Kidney sections were stained for
MAGL (green) and Fibronectin (red) by immunofluorescence. Arrows indicate positive
staining. Scale bar, 50 μ m.

Figure 5. MAGL effectively inhibits TGF- β 1-induced lipotoxicity and fibrosis in tubular cells

A. Representative graph showing the construction of tubular cell specific MAGL knock-in mice
(Rosa26-MAGL-CKI). **B.** Experimental design. Primary tubular epithelial cells were isolated
from wildtype mice or MAGL-CKI mice, and then treated with Saline or TGF- β 1 (5 ng/ml) for
24 h. **C.** Representative micrographs showing freshly isolated tubules and cultured primary
tubular cells in bright field. Scale bar, 100 μ m. **D-E.** Representative western blot and
quantitative data showing the expression of MAGL in different groups. Primary tubular
epithelial cells isolated from wildtype mice were treated with TGF- β 1 (5 ng/ml) for indicated
time period (0, 3, 6, 12, 24 h). Numbers (1 – 2) indicate each individual culture in a given group.
n.s., ****P* < 0.001 versus the control group. n = 3. n.s.: none of significance. **F-G.**
Representative western blot and quantitative data showing the expression of MAGL, CB2 and
Active- β -catenin in different groups. **P* < 0.05, ***P* < 0.01, ****P* < 0.001 versus the control
group alone; #*P* < 0.05, ###*P* < 0.001 versus the TGF- β 1 treatment group alone. n = 3. **H-L.**
Representative western blot and quantitative data showing the expression of PGC-1 α , PPAR α ,

CPT1A and Fibronectin in different groups. $*P < 0.05$, $***P < 0.001$ versus the control group alone; $^{##}P < 0.01$, $^{###}P < 0.001$ versus the TGF- β 1 treatment group alone. $n = 3$. **M.** Representative immunofluorescence micrographs showing the expression of Fibronectin and lipid (Nile Red) in different groups. White arrows indicate positive staining. Scale bar, 25 μ m. **N.** HK-2 cells were pretreated with recombinant MAGL protein (100 ng/ml) for 1 h, and then treated with TGF- β 1 (5 ng/ml) for 24 h. **O-R.** Representative western blot and quantitative data showing the expression of MAGL, CB2 and β -catenin in different groups. Numbers (1 – 3) indicate each individual culture in a given group. $*P < 0.05$, $***P < 0.001$ versus the control group alone; $^{#}P < 0.05$, $^{##}P < 0.01$, $^{###}P < 0.001$ versus the TGF- β 1 treatment group alone. $n = 3$. **S.** Representative immunofluorescence micrographs showing the expression of lipid (Nile Red) and Fibronectin in different groups. White arrows indicate positive staining. Scale bar, 25 μ m. **T-W.** Representative western blot and quantitative data showing the expression of CPT1A, PPAR α , and Fibronectin in different groups. Numbers (1 – 3) indicate each individual culture in a given group. $*P < 0.05$ versus the control group alone; $^{#}P < 0.05$, $^{##}P < 0.01$ versus the TGF- β 1 treatment group alone. $n = 3$.

Figure 6. Specially knock-in of MAGL in tubular cell inhibits CB2/ β -catenin signaling in FAN mice

A. Experimental design. White bar and green bar indicate wildtype mice were administered intraperitoneal injections of saline or folic acid at 250 mg/kg. Red bar indicates Rosa26-MAGL-CKI mice were administered intraperitoneal injections of folic acid at 250 mg/kg. Mice were sacrificed at 10 d after injection. FA: folic acid. MAGL-CKI: tubular cell specific MAGL knock-in mice. **B.** Quantitative data showing renal mRNA levels of MAGL in different groups.

918 *** $P < 0.001$ versus the wildtype control group alone; ### $P < 0.001$ versus the FA treatment
919 group alone. $n = 5$. **C-D.** Representative western blot and quantitative data showing the
920 expression of MAGL in different groups. Numbers (1 – 3) indicate each individual animal in a
921 given group. *** $P < 0.001$ versus the wildtype control group alone; ### $P < 0.001$ versus the FA
922 treatment group alone. $n = 5$. **E.** Representative immunofluorescence micrographs showing
923 renal expression of MAGL in different groups. White arrows indicate positive staining. Scale
924 bar, 50 μm . **F-G.** Representative graphs showing Scr and BUN levels in different groups. * $P <$
925 0.05 versus the wildtype control group alone; # $P < 0.05$ versus the FA treatment group alone. n
926 = 5. **H.** Representative graph showing 2-AG levels in kidney homogenates by LC/MS analysis.
927 *** $P < 0.001$ versus the wildtype control group alone; ### $P < 0.001$ versus the FA treatment
928 group alone. $n = 5$. **I.** Gene expression profiling heatmap by RNA-seq showing differential gene
929 clustering of kidneys from different groups. Numbers (1 – 3) indicate each individual animal in
930 a given group. **J.** Gene ontology (GO) analysis showing differentially expressed genes (DEGs)
931 in 2 groups. Red color indicates the upregulation of biological processes, while blue color
932 indicates the downregulation. **K-N.** Gene set enrichment analysis (GSEA) enrichment plots
933 showing the different enrichment of genes in FA treatment group compared to sham group mice
934 alone or FA/MAGL -CKI group compared to FA treatment group mice alone. P value < 0.05 .
935 NES: normalized enrichment score. **O-R.** Representative western blot and quantitative data
936 showing the expression of CB2, CB1 and Active- β -catenin in different groups. Numbers (1 –
937 3) indicate each individual animal in a given group. ** $P < 0.01$, *** $P < 0.001$ versus the
938 wildtype control group alone; n.s., ## $P < 0.01$ versus the FA treatment group alone. $n = 5$. n.s.:
939 none of significance. **S.** Quantitative data showing renal mRNA levels of CB2 in different

groups. $***P < 0.001$ versus the wildtype control group alone; $###P < 0.001$ versus the FA treatment group alone. $n = 5$. **T.** Representative micrographs showing renal expression of CB2 and β -catenin in different groups. White arrows indicate positive staining. Scale bar, 50 μm .

Figure 7. Tubular cell specific MAGL knock-in mice resist lipid deposition and renal fibrosis in FAN model

A. Representative micrographs showing the expression of PPAR α and CPT1A in kidney. Arrows indicate positive staining. For PPAR α staining, scale bar 25 μm ; for CPT1A staining, scale bar, 50 μm . **B-F.** Representative western blot and quantitative data showing the expression of PGC-1 α , PPAR α , CPT1A and ACOX1 in different groups. Numbers (1 – 3) indicate each individual animal in a given group. $*P < 0.05$, $**P < 0.01$, $***P < 0.001$ versus the wildtype control group alone; $^{\#}P < 0.05$, $^{\#\#}P < 0.01$, $^{\#\#\#}P < 0.001$ versus the FA treatment group alone. $n = 5$. **G-L.** Quantitative data showing renal mRNA levels of PGC-1 α , PPAR α , CPT1A, CPT2, ACOX1 and ACOX2 in different groups. $***P < 0.001$ versus the wildtype control group alone; n.s. $^{\#}P < 0.05$, $^{\#\#}P < 0.01$, $^{\#\#\#}P < 0.001$ versus the FA treatment group alone. $n = 5$. n.s.: none of significance. **M.** Representative micrographs showing the expression of lipid (Nile Red) and ADRP in kidney. Arrows indicate positive staining. Scale bar, 25 μm . **N.** Representative TEM images showing lipid droplets in renal tubular epithelial cells in different groups. Yellow arrows indicate lipid droplets. Scale bar, 1 μm . **O.** Representative graph showing renal triglyceride levels in different groups. $*P < 0.05$ versus the wildtype control group alone; $^{\#}P < 0.05$, versus the FA treatment group alone. $n = 5$. TG: triglyceride. **P.** Representative micrographs showing PAS and Sirius Red staining. Black arrows indicate injury tubules or fibrotic area. Scale bar, 50 μm . **Q-R.** Quantitative analysis of tubular injury and positive staining of fibrotic area in

different groups as indicated. Kidney sections were subjected to PAS staining or Sirius Red staining. At least 10 randomly selected fields were evaluated under $400\times$ magnification and results were averaged for each animal. $**P < 0.01$, $***P < 0.001$ versus the wildtype control group alone; $^{##}P < 0.01$ versus the FA treatment group alone. $n = 5$. **S-U.** Representative western blot and quantitative data showing the expression of Fibronectin and α -SMA in different groups. Numbers (1 – 3) indicate each individual animal in a given group. $*P < 0.05$, $**P < 0.01$ versus the wildtype control group alone; $^{\#}P < 0.05$, $^{##}P < 0.01$ versus the FA treatment group alone. $n = 5$.

Figure 8. Supplement of recombinant MAGL effectively protects against renal fibrosis in UIRI mice

A. Experimental design. Mice were performed UIRI or sham surgery. Red bar indicates intravenous injections of recombinant MAGL protein ($4\text{ }\mu\text{g/kg/d}$) or vehicle. Mice were subjected to unilateral nephrectomy at 10 d and sacrificed at 11 d after UIRI surgery. UNX: unilateral nephrectomy. **B-D.** Representative graphs showing ACR, Scr and BUN levels in different groups. $***P < 0.001$ versus the sham control group alone; $^{##}P < 0.01$, $^{###}P < 0.001$ versus the UIRI group alone. $n = 5$. **E-F.** Representative graphs showing 2-AG levels in serum and kidney homogenates by LC/MS analysis. $**P < 0.01$, $***P < 0.001$ versus the sham control group alone; $^{###}P < 0.001$ versus the UIRI group alone. $n = 5$. **G.** Representative micrographs showing renal expression of MAGL and β -catenin in different groups. White arrows indicate positive staining. For MAGL staining, scale bar, $50\text{ }\mu\text{m}$; for β -catenin staining, scale bar, $75\text{ }\mu\text{m}$. **H-L.** Representative western blot and quantitative data showing the expression of MAGL, CB2,

CB1 and Active- β -catenin in different groups. Numbers (1 – 3) indicate each individual animal in a given group. $**P < 0.01$, $***P < 0.001$ versus the sham control group alone; n.s., $^{##}P < 0.01$, $^{###}P < 0.001$ versus the UIRI group alone. n = 5. n.s.: none of significance. **M-Q.** Representative western blot and quantitative data showing the expression of PGC-1 α , PPAR α , CPT1A and ACOX1 in different groups. Numbers (1 – 3) indicate each individual animal in a given group. $*P < 0.05$, $***P < 0.001$ versus the sham control group alone; $^{#}P < 0.05$, $^{###}P < 0.001$ versus the UIRI group alone. n = 5. **R.** Representative micrographs showing renal expression of ADRP, lipid (Nile Red) and PPAR α in different groups. Arrows indicate positive staining. For ADRP and PPAR α , scale bar, 50 μ m; for Nile Red, scale bar, 25 μ m. **S-T.** Representative western blot and quantitative data showing the expression of Fibronectin in different groups. Numbers (1 – 3) indicate each individual animal in a given group. $**P < 0.01$ versus the sham control group alone; $^{##}P < 0.01$ versus the UIRI group alone. n = 5. **U.** Representative micrographs showing Sirius Red staining and PAS staining. Black arrows indicate fibrotic area or injury tubules. Scale bar, 50 μ m. **V-W.** Quantitative analysis of positive staining of fibrotic area and tubular injury in different groups as indicated. Kidney sections were subjected to Sirius Red staining or PAS staining. At least 10 randomly selected fields were evaluated under 400 \times magnification and results were averaged for each animal. $***P < 0.001$ versus the wildtype control group alone; $^{###}P < 0.001$ versus the FA treatment group alone. n = 5.

Figure 9. 2-AG suppresses PPAR α /PGC-1 α -mediated FAO via β -catenin signaling

A-D. Representative western blot and quantitative data showing the expression of CB2, CB1 and β -catenin in HK-2 cells treated with 2-AG (100 μ M) for 24 h. Numbers (1 – 3) indicate

each individual culture in a given group. n.s., $*P < 0.05$, $**P < 0.01$ versus the control group alone. n = 3. n.s.: none of significance. **E.** Representative micrographs showing colocalization of CB2 (red) and 2-AG (green) in HK-2 cells. HK-2 cells were treated with 2-AG (100 μ M) packaged with indocyanine green material for 2 h. White arrow indicates the colocalization of 2-AG and CB2. Scale bar, 10 μ m. **F.** Seahorse analysis of HK-2 cells reveals distinct metabolic profiles across 3 groups: CTL, 2-AG (100 μ M), and 2-AG (100 μ M) cotreatment with MAGL (100 ng/ml). The cells were treated with etomoxir (ETO), oligomycin, FCCP, rotenone and antimycin (Rot / AA) during the assay. OCR was measured to assess cellular respiration. **G-I.** Quantitative data showing the differences in basal respiration, maximal respiration, and ATP production. $**P < 0.01$, $***P < 0.001$ versus control group alone; $^{##}P < 0.01$ versus 2-AG group alone. n = 3. **J.** Representative western blot showing the expression of PGC-1 α , PPAR α , CPT1A and ACOX1 in 2 groups. Numbers (1 – 3) indicate each individual culture in a given group. n = 3. **K-M.** Representative western blot and quantitative data showing the expression of β -catenin in cytosolic and nuclear fractions. HK-2 cells were treated with 2-AG (100 μ M) for 24 h. The cytosolic and nuclear fractions were isolated and detected by western blot. The expression of cytosolic and nuclear proteins was normalized to α -tubulin and TATA binding protein (TBP) respectively. Numbers (1 – 3) indicate each individual culture in a given group. $**P < 0.01$, $***P < 0.001$ versus control group alone. n = 3. **N-O.** Representative western blot showing β -catenin decreased the binding of PGC-1 α and PPAR α . HK-2 cells were transfected with β -catenin expression plasmid (pFlag- β -catenin) or pcDNA3.1(+) for 24 h. Cell lysates were immunoprecipitated (IP) with antibodies against PGC-1 α or PPAR α , followed by immunoblotting (IB) with PPAR α or PGC-1 α . **P-Q.** Representative western blot showing ICG-

001 reversed 2-AG-blocked binding of PGC-1 α and PPAR α . HK-2 cells were treated with 2-AG (100 μ M) alone or treated with ICG-001 (10 μ M) for 24 h. Cell lysates were immunoprecipitated (IP) with antibodies against PGC-1 α or PPAR α , followed by immunoblotting (IB) with PPAR α or PGC-1 α . **R-V.** Representative western blot and quantitative data showing the expression of Flag, PGC-1 α , PPAR α and ACOX1 in HK-2 cells transfected with β -catenin expression plasmid (pFlag- β -catenin) or pcDNA3.1(+) for 24 h. Numbers (1 – 3) indicate each individual culture in a given group. * P < 0.05, ** P < 0.01 versus the pcDNA3.1(+) group alone. n = 3. **W.** Experimental design. Primary tubular epithelial cells were isolated from β -catenin loxp/loxp mice and transfected with Adv-CMV-Cre virus to knock out β -catenin and then treated with 2-AG (100 μ M) for 24 h. **X.** Representative western blot showing the expression of β -catenin, E-cadherin, PGC-1 α , PPAR α , CPT1A and Fibronectin in different groups. Numbers (1 – 3) indicate each individual culture in a given group. n = 3. **Y.** Representative immunofluorescence micrographs showing the expression of E-cadherin, lipid (Nile Red) and Fibronectin in different groups. White arrows indicate positive staining. For E-cadherin and Nile Red staining, scale bar, 25 μ m; for Fibronectin staining, scale bar, 50 μ m. **Z.** The schematic diagram demonstrates 2-AG binds to the receptor CB2 to induce β -catenin activation and then inhibits transcriptional activity of PGC-1 α /PPAR α to block FAO-related genes expression, which results in lipid accumulation and subsequent fibrogenesis. Of note, MAGL could hydrolyze 2-AG to block the whole pathway, and then ameliorates lipid toxicity and fibrogenesis in renal tubular cells.

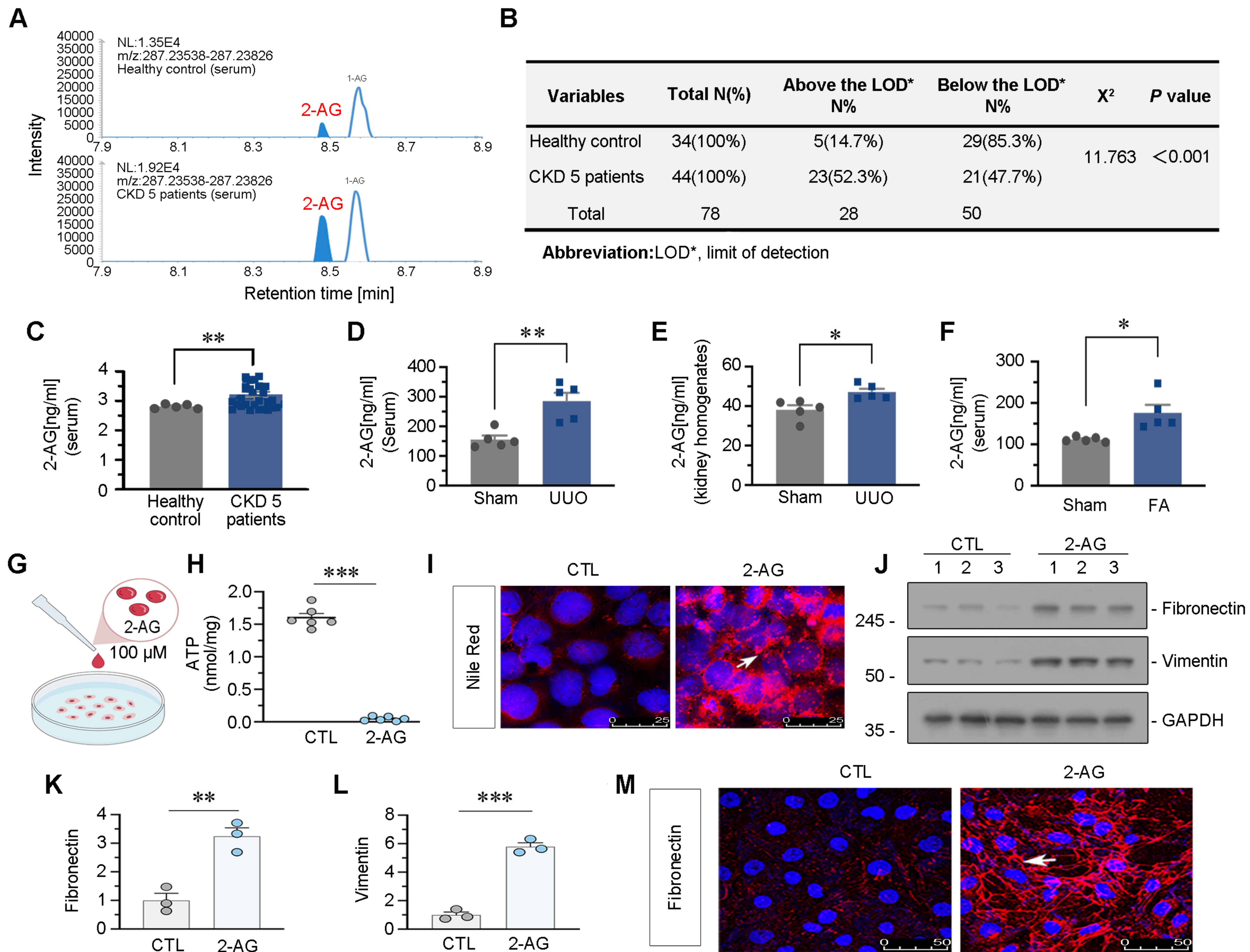


Figure 1

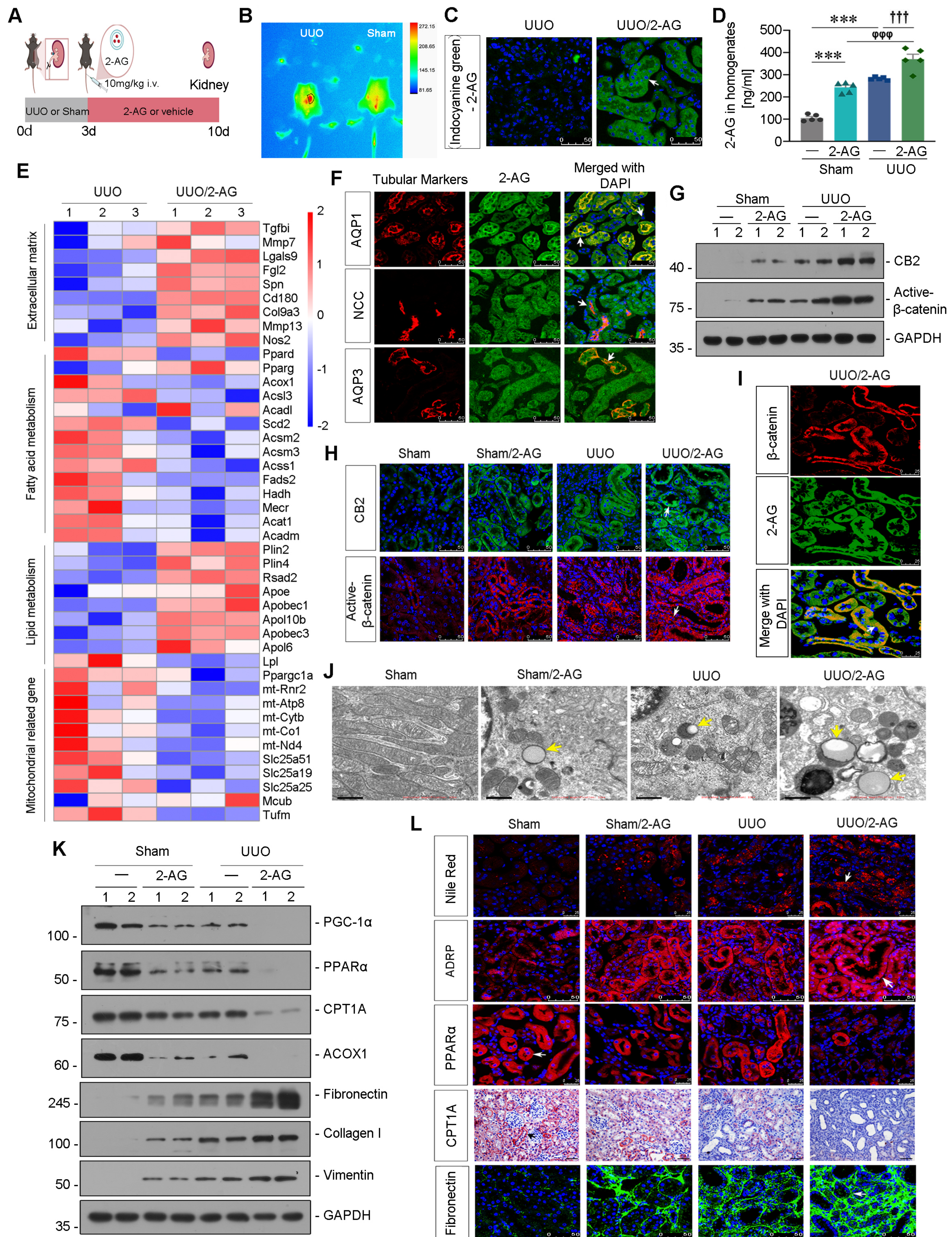


Figure 2

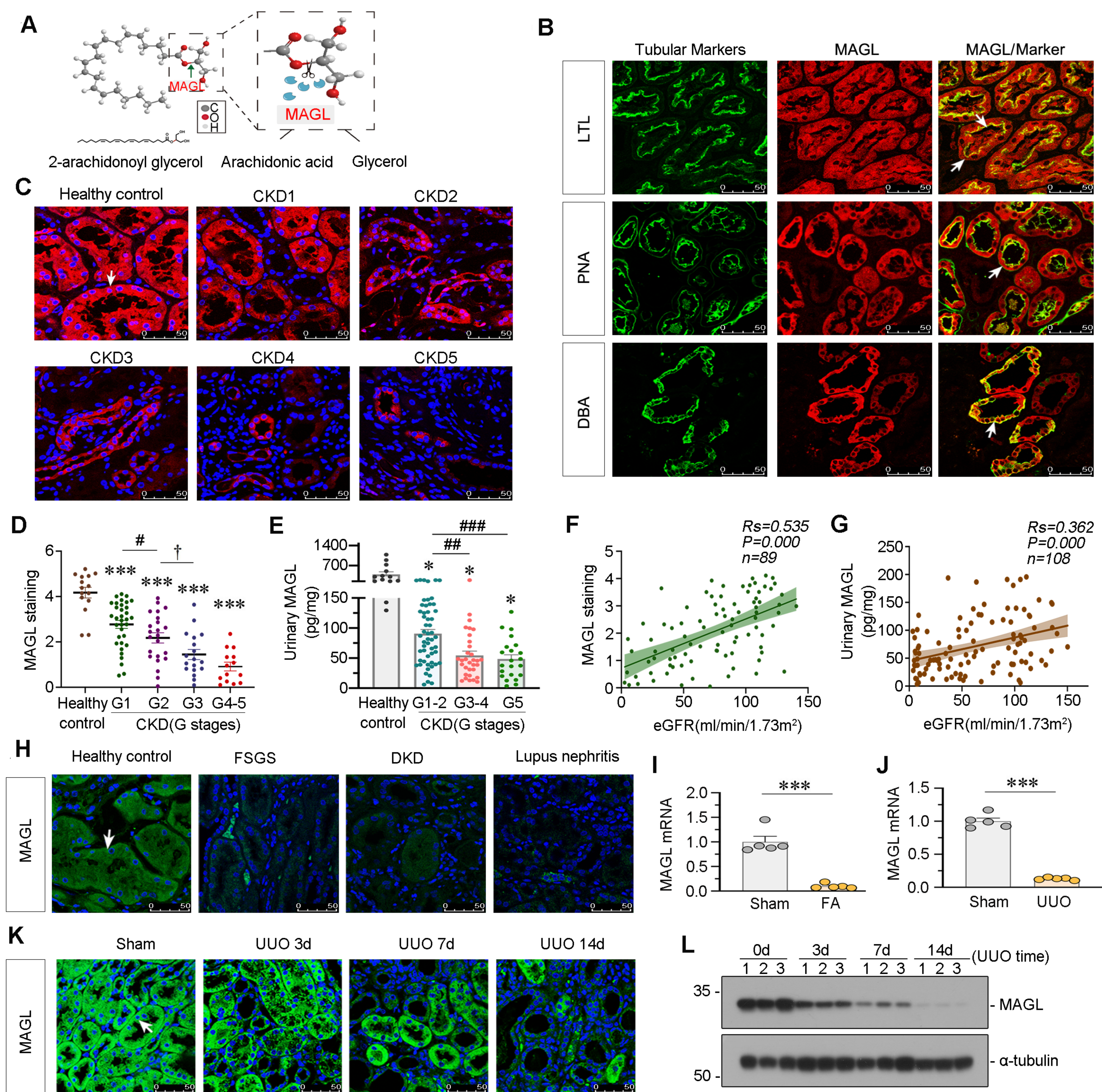


Figure 3

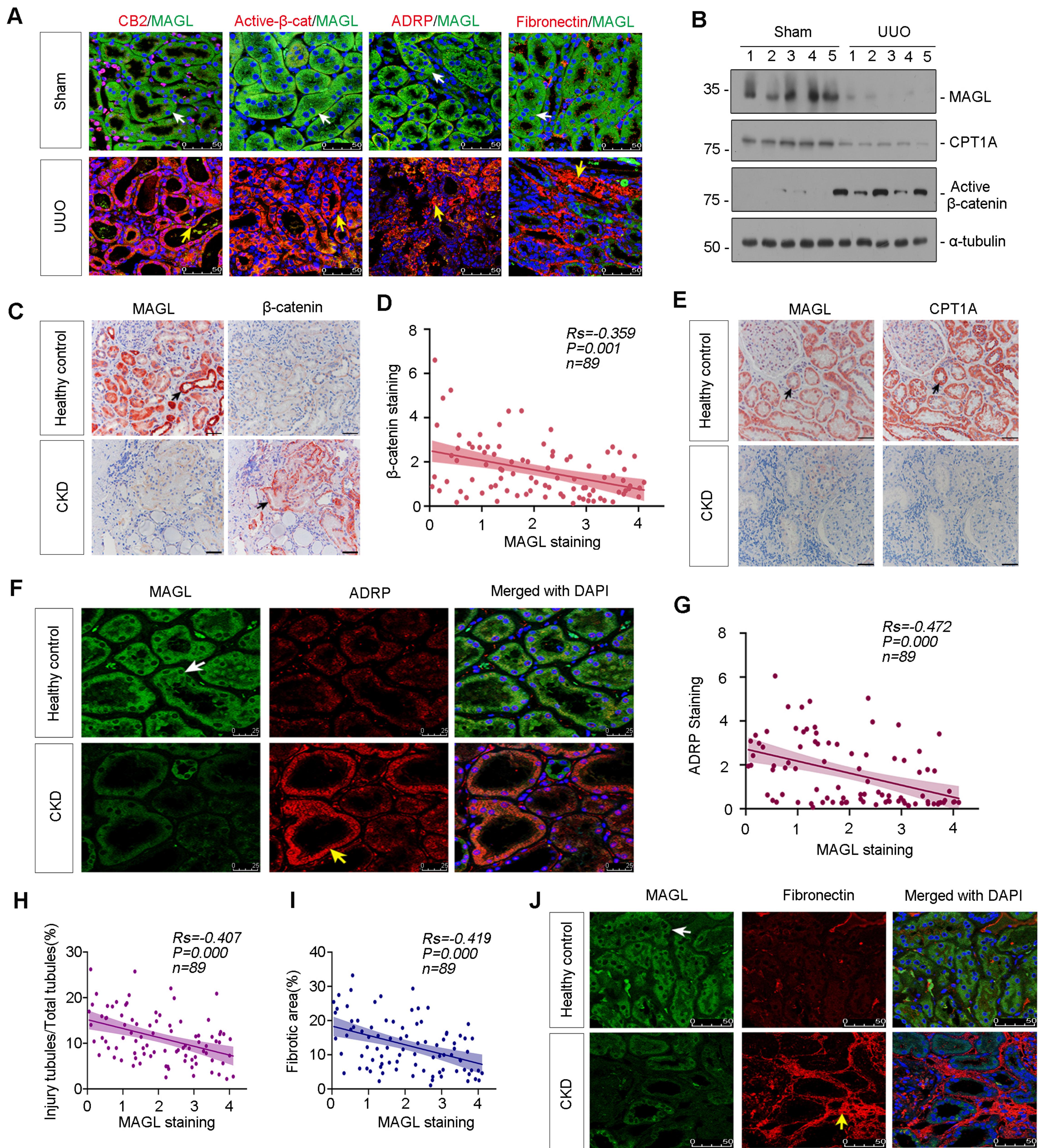


Figure 4

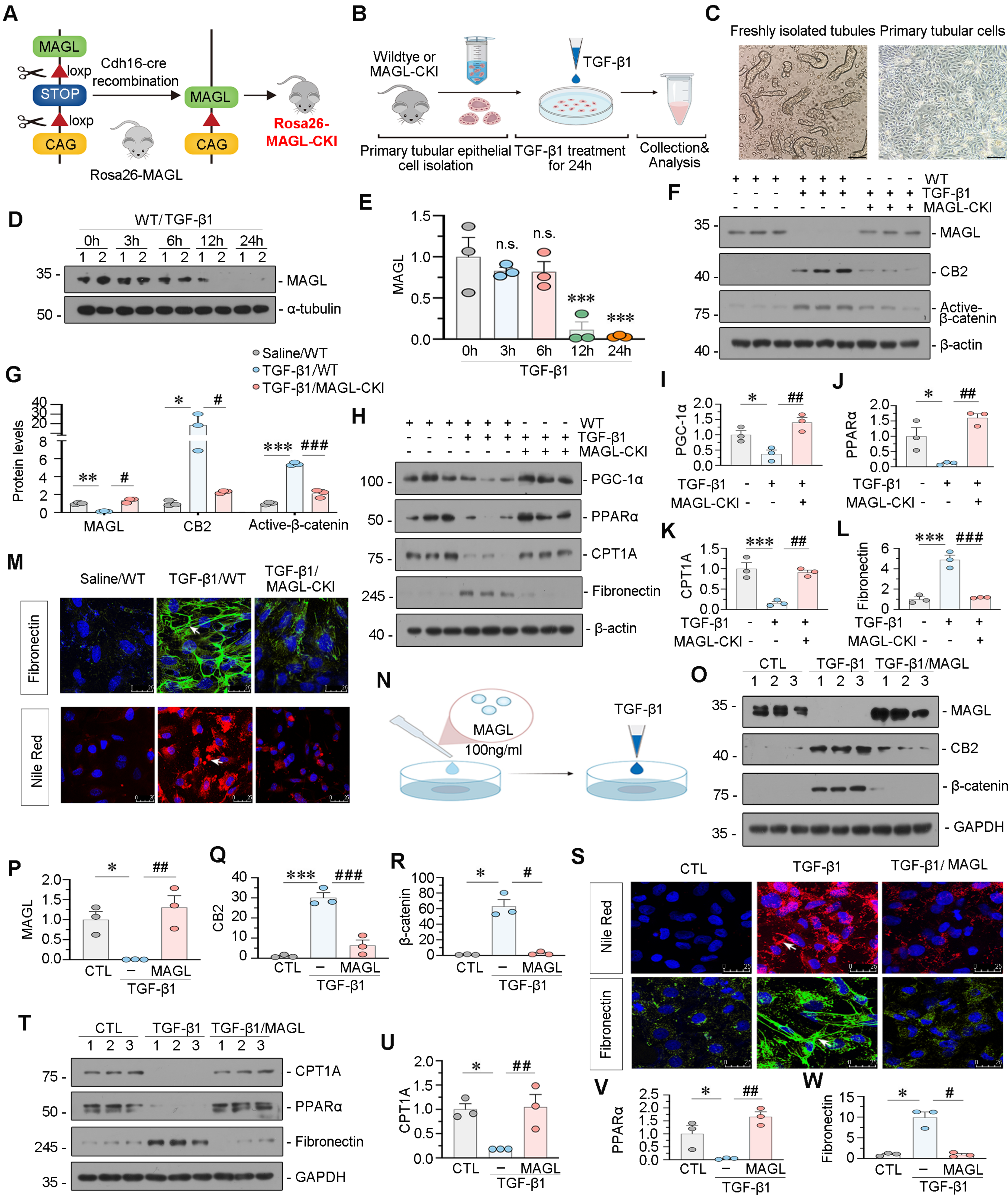


Figure 5

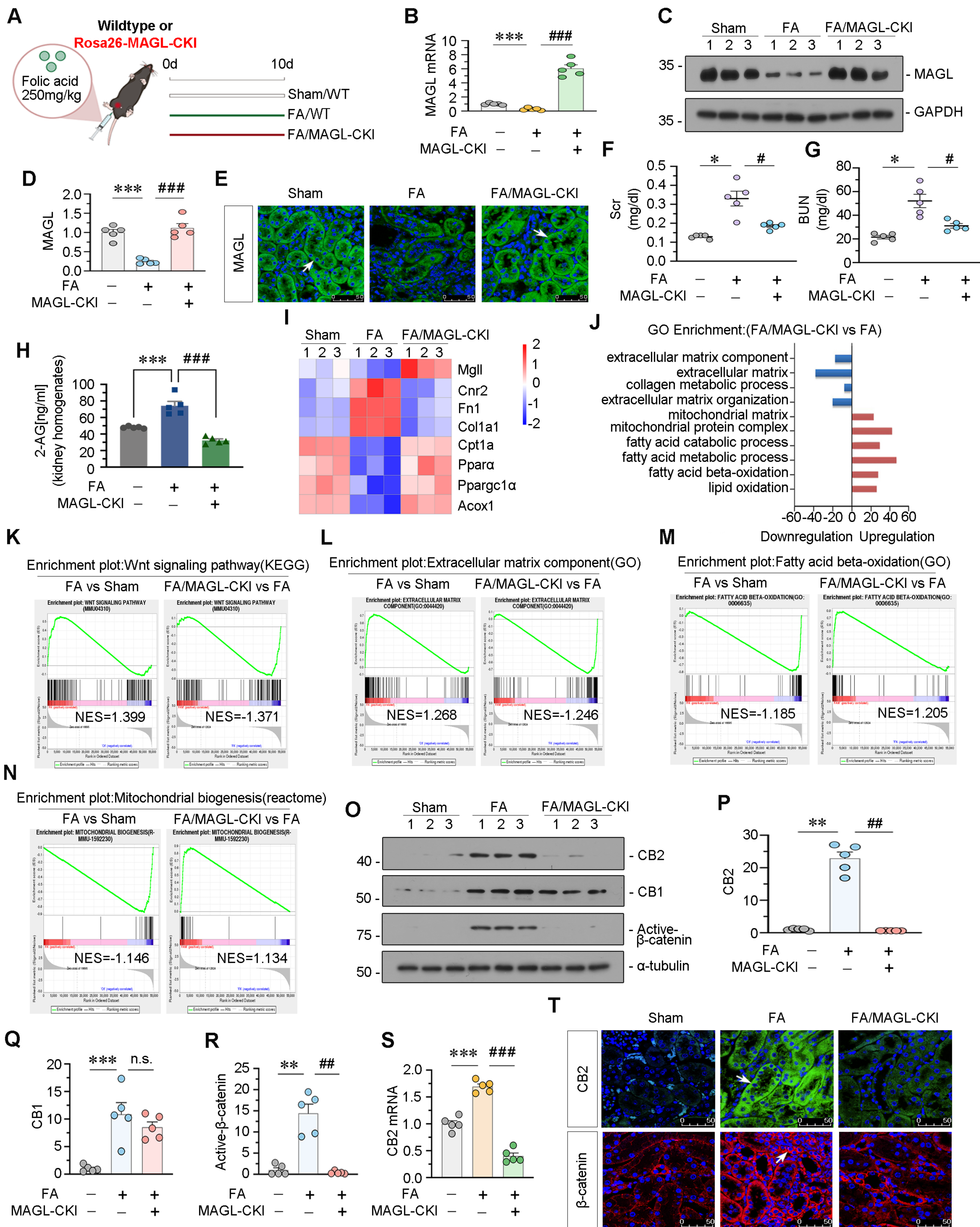


Figure 6

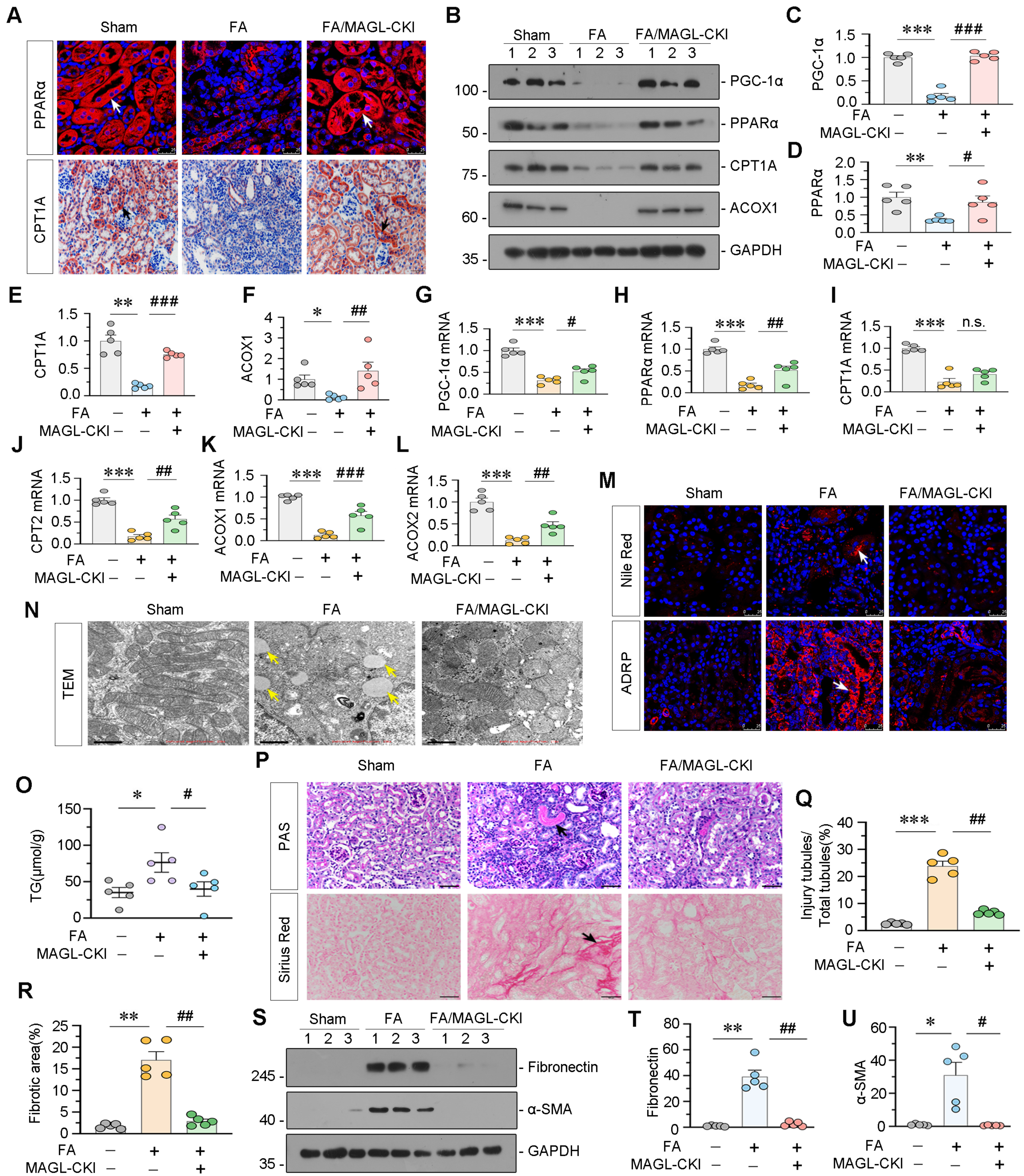


Figure 7

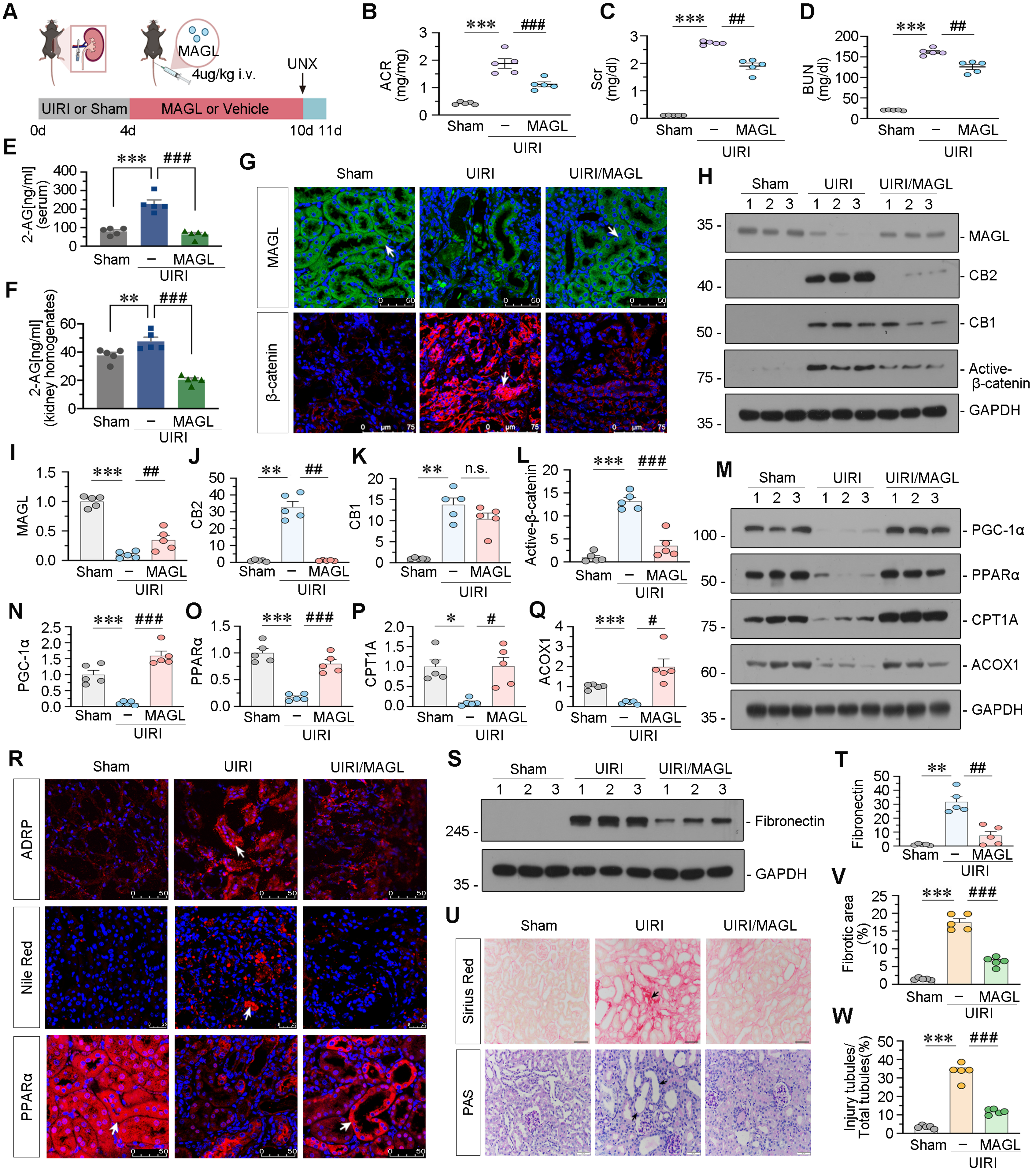


Figure 8

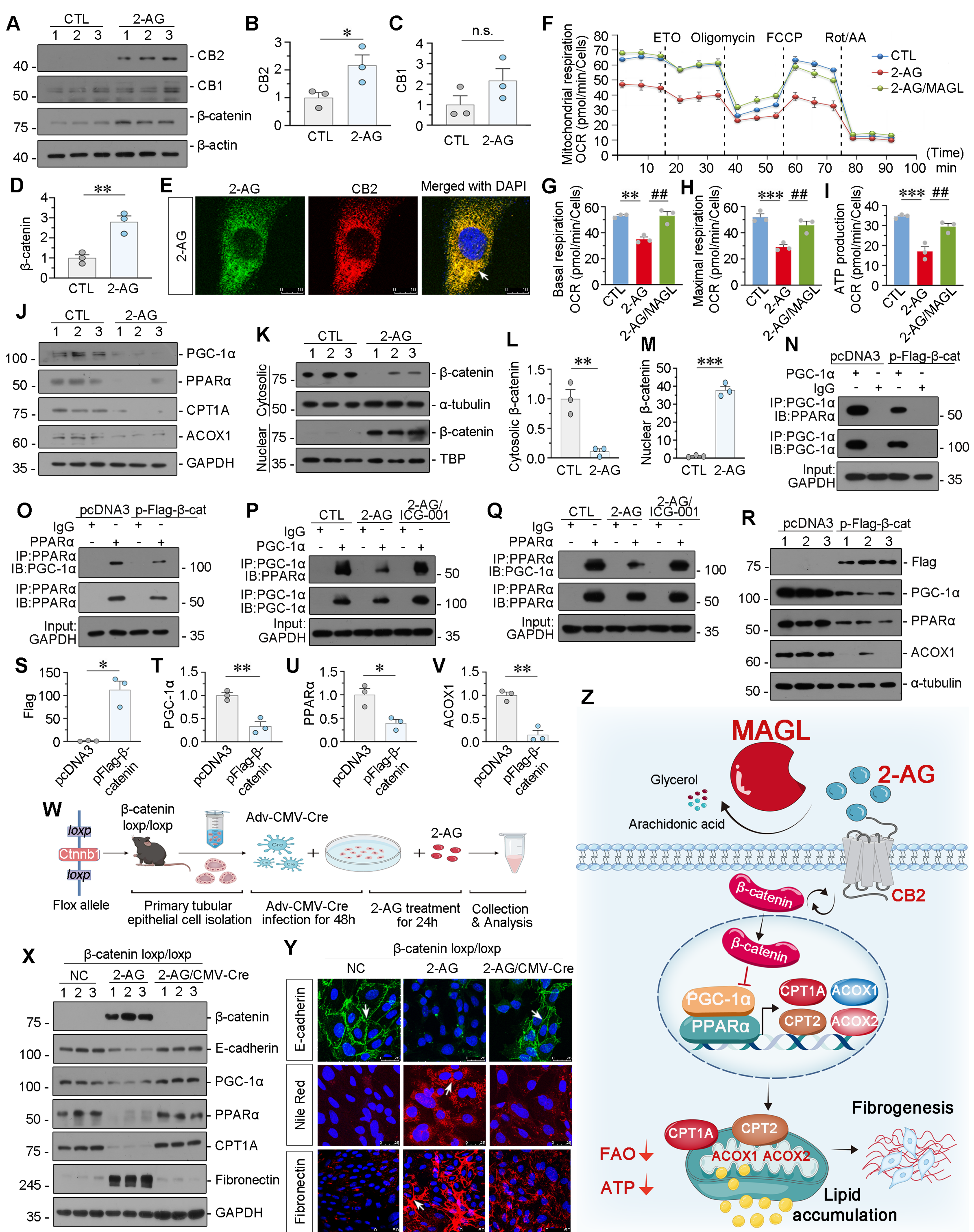


Figure 9

1

2

3

4

9

11

13

14

15

Supplementary Detail Methods

Human clinical specimens

All human specimens (urine, serum and kidney biopsies) were collected from patients with CKD at the First People's Hospital of Foshan. CKD was diagnosed based on an estimated glomerular filtration rate (eGFR). 24 h urine and serum samples were collected in cryotubes respectively and stored at -80 °C. Normal control biopsies were obtained from paracancerous tissues of patients who had renal cell carcinoma and underwent nephrectomy. The demographic and clinical data are presented in Supplementary Table. All the studies involving human samples were performed with informed patient consent and approved by the Medical Ethics Committee of the First People's Hospital of Foshan (FSYYY – EC – SOP – 008 - 02.0 - A09).

MAGL enzyme-linked immunosorbent assay

The urinary concentration of MAGL was analyzed by human Monoglyceride lipase ELISA kit (CSB - EL013787HU; CUSABIO Life Science, Wuhan, China) and corrected by urine creatinine.

Animal models

Male C57BL/6 mice weighing 20 – 22 g were purchased from the Experimental Animal Center of Southern Medical University (Guangzhou, China). Tubule-specific MAGL conditional knock-in mice were purchased from Cyagen Biosciences. All mice undergoing surgeries were treated with general anesthesia and housed in Experimental Animal Center of Southern Medical University under pathogen-free conditions.

For studying the effects of 2-AG, the UUO model was established by triple-ligating the left ureter with 4-0 silk after an abdominal midline incision. At 3 d after operation, mice were subjected to daily intravenous injections of 2-AG Nanoparticles for 7 d in the dark room. Mice were sacrificed at 10 d

after UUO surgery. Mice have randomly divided into 4 groups: (i) sham controls; (ii) mice treated with 2-AG; (iii) UUO mice treated with vehicle; (iv) UUO mice treated with 2-AG.

For the folic acid–induced nephropathy model, mice were administered a single intraperitoneal injection of folic acid at 250 mg/kg body weight. Tubule-specific MAGL conditional knock-in mice and matched C57BL/6 mice were sacrificed at 10 d after FA injection.

For the UIRI model, the left renal pedicle was clipped for 35 min using microaneurysm clamps. At 4 d after operation, mice were daily injected intravenously with Recombinant Human MAGL Protein (Catalog: 7930-MG; R&D Systems) at 4 µg/kg through the tail vein for a week by a hydrodynamic-based gene delivery approach. After 10 d post-IRI, the right kidney was removed via a right flank incision. Mice were sacrificed at 11 d post-IRI, respectively. Mice have randomly divided into 3 groups: (i) sham controls; (ii) UIRI mice treated with vehicle; (iii) UIRI mice treated with Recombinant Human MAGL Protein.

The detailed experimental designs were shown in Figures 2A, 6A, 8A.

For ADR model, male BALB/c mice were treated with ADR via a single intravenous injection of 11 mg/kg body weight. Mice were killed at 1, 3 and 5 w after ADR injection.

All mice were randomly divided into different groups as indicated, using the online tool “Research Randomizer” (<https://www.randomizer.org>). 5 mice were included in each group. All animal studies were performed in accordance with the Guidelines for the Care and Use of Laboratory Animal and approved by the Animal Ethics Committee at the Nan fang Hospital, Southern Medical University (NFYY-2020- 0837).

Generation of β -catenin loxp/loxp mice

The β -catenin loxp/loxp mice were generated in C57BL/6 background by CRISPR/Cas9 system and were purchased from Cyagen Biosciences (stock no. CKOCMP - 12387 - Ctnnb1 - B6N - VA; Cyagen Biosciences, Guangzhou, China). The genotyping of tail DNA samples was confirmed by RT-PCR.

Tubule-specific MAGL conditional knock-in mice and genotyping

The construction of MAGL-CKI was achieved by applying CRISPR/Cas9 for the knock-in of MAGL gene into Rosa26 of C57BL/6 zygotes. Cdh16-cre recombinase removed the stop signal (a translation interrupting Loxp-Stop-Loxp cassette) between the loxP sites. A high level of MAGL expression was driven by the CAG promoter.

The MAGL-CKI transgenic mice were purchased from Cyagen Biosciences (TIS190827MG1; Cyagen Biosciences, Guangzhou, China). The genotyping of tail DNA samples was confirmed by RT-PCR.

Urinary albumin, serum creatinine and BUN assay

Serum creatinine and BUN levels were determined by an automatic chemistry analyzer (AU480 Chemistry Analyzer, Beckman Coulter, Atlanta, Georgia). The data were expressed as mg/dl. Urinary albumin was measured using a mouse Albumin ELISA Quantitation kit (Bethyl Laboratories, Montgomery, TX), and standardized to urine creatinine.

Preparation of 2-AG Nanoparticles

Liposome containing DPPC : DSPE-PEG2000 = 95:5 (molar ratio) was prepared by the reported thin film hydration method¹. Normally, lipid: 2-AG = 20 : 1 (weight ratio) was fully dissolved in 30 ml

CHCl₃, and CHCl₃ was removed by rotary evaporation at 25 °C until a thin lipid film was formed. Residual solvent in liposome was removed in vacuum for 6 h. A PBS solution of indocyanine green (ICG) (500 µg/ml, Apexbio) was added to the lipid film, and ICG was encapsulated by rotary evaporation at 25 °C. The crude liposome was extruded through a 100 nm filter for 11 times using an Avanti Polar Lipids mini-extruder (Alabaster, AL).

***In vivo* Bioimaging of 2-AG distribution**

C57BL/6 mice were subjected to sham or UUO surgery. 3 d after surgery, mice were intravenously injected with 2-AG-loaded nanoparticles at 10 mg/kg body weight after general anesthesia. 2 h later, the anesthetized mice were placed into the chamber, and the fluorescence images were visualized using a Bruker FX PRO imaging system equipped with an excitation at 785 nm and emission at 810 nm. All procedures were conducted in dark.

Nuclear and cytoplasmic fraction isolation

Nuclear and cytoplasmic fractions were separated with a commercial kit (BB-3102; BestBio, Shanghai, China) according to the manufacturer's protocol.

Isolation of tubular epithelial cells and treatment

Primary mouse kidney tubular epithelial cells were isolated and cultured using routine protocol. Briefly, the kidneys of β -catenin loxp/loxp mice or tubule-specific MAGL conditional knock-in mice were peeled off and minced, then digested with 0.75 mg/ml collagenase (Cat No 4188; Worthington) for 25 min at 37 °C.

The tubular tissues were isolated by 100 μ m cell filter and then they were centrifuged using 31% Percoll gradients, resuspended and washed twice with DMEM/F-12. Finally, tubules were suspended in DMEM/F-12 supplemented with 10% bovine calf serum, 50 U/ml penicillin and 50 mg/ml streptomycin. Cells were grown in cell culture dishes for 4-8 d until they reached about 60% confluency.

The primary renal tubular epithelial cells isolated from β -catenin loxp/loxp mice were transfected with Adv-CMV-Cre (GCD0320409; Genechem Shanghai, China) for 48 h according to the manufacturer's protocol. Then 2-AG at 100 μ M was added into the cells for another 24 h.

The primary renal tubular epithelial cells isolated from tubule-specific MAGL conditional knock-in mice were treated with TGF- β 1 (5 ng/ml) for 24 h.

The cells were harvested for immunofluorescence and protein analyses.

Cell Culture and Treatment

HK-2 was purchased from the Cell Bank of the Chinese Academy of Sciences (Shanghai, China) and cultured in DMEM/F12 medium (Biological Industries) supplemented with 10% fetal bovine serum (Biological Industries). No contamination was detected.

HK-2 cells were synchronized into quiescence by growing in serum-free medium, and then treated with 2-AG (100 μ M, Catalog No. 1298; Tocris Bioscience) for 24 h. Some cells were pretreated with recombinant MAGL protein (100 ng/ml, Catalog No. 7930-MG; R&D) for 1 h, and then treated with TGF- β 1 (5 ng/ml, Catalog No. 7754-BH; R&D) for 24 h. In some experiments, HK-2 cells were treated with TGF- β 1 (5 ng/ml) alone or cotreated with JZL-184 (20 μ mol/ml, ab141592; Abcam) for 24 h.

Seahorse assay

HK-2 cells (50,000 cells/well) were seeded in Seahorse XF96 cell culture microplates and subjected to various treatments (2-AG alone or in combination with MAGL). Following a 1-hour incubation in Seahorse XF DMEM medium supplemented with 10 mM XF glucose solution, 1 mM XF sodium pyruvate solution, and 2 mM glutamine solution, baseline measurements of basal OCR were recorded using a Seahorse XF96 Analyzer. To assess mitochondrial function, sequential injections of oligomycin (1.5 μ M), FCCP (1 μ M), rotenone and antimycin (0.5 μ M) were administered, providing insights into maximal OCR and mitochondrial respiratory parameters. To evaluate FAO, Etomoxir (4 μ M) was introduced. All reagents were provided by Agilent Technologies as part of the Seahorse XF Cell Mito Stress Test Kit (Catalog Number: 103674 - 100). The collected data were meticulously analyzed to elucidate cellular metabolism and energy production, offering a comprehensive understanding of metabolic dynamics under different experimental conditions.

Western blot analysis

Protein expression was analyzed by western blot analysis. Briefly, total proteins were extracted from renal tissues and cell pellets with lysis buffer. Protein concentration were measured using BCA protein concentration determination. Proteins were subjected to SDS-PAGE electrophoresis and transferred to polyvinylidene difluoride (PVDF) membrane (Merck Millipore Ltd, IPVH00010, Ireland), then blocked in 5% of milk and incubated with different primary antibodies at 4 °C overnight. The next day, PVDF membrane was incubated with a responding secondary antibody for 1 h at room temperature, and visualized by an ECL kit (Applygen, Beijing, China). The primary antibodies used were as follows: anti-CB2 (ab45942; Abcam), anti-Fibronectin (F3648; Sigma), anti- α -SMA (a2547; Sigma-Aldrich), anti- α -SMA (ab5694; Abcam), anti- β -catenin (610154; BD Biosciences), anti-PGC-1 α (ab54481;

Abcam), anti-TOMM20 (ab186735; Abcam), anti- α -tubulin (RM2007; Ray Antibody Biotech), anti-GAPDH (RM2002; Ray Antibody Biotech), anti- β -actin (RM2001; Ray Antibody Biotech), anti-Collagen I (BA0325; Boster, Biotechnology), anti-CB1 (BA2144; Boster Biotechnology), anti-Active- β -catenin (4270s; Cell Signaling Technology), anti-CPT1A (ab128568; Abcam), anti-ACOX1 (A8091; ABclonal), anti-PPAR α (A18252; ABclonal), anti-Flag-tag (M185-3; MBL), anti-TBP (ab818; Abcam), anti-MAGL (ab228598; Abcam), anti-E-cadherin (ab76055; Abcam), anti-Vimentin (5741s; Cell Signaling Technology).

Immunoprecipitation

The protein-protein interaction was assessed by co-immunoprecipitation as previously described². HK-2 cells were pretreated with ICG-001 (10 μ M) before treated with 2-AG (100 μ M) or transfected with β -catenin expression plasmid (pFlag- β -catenin) alone. Cell lysates were immunoprecipitated with antibodies against anti-PPAR α (A18252; ABclonal) or anti-PGC-1 α (ab54481; Abcam), followed by immunoblotting with anti-PPAR α (A18252; ABclonal), and anti-PGC-1 α (ab54481; Abcam).

Triglycerides (TG) assay

Triglycerides was tested using a commercial kit (E1025-105; APPLYGEN) according to the manufacturer's protocol.

Nile Red Staining

Kidney cryosections or HK-2 cells cultured on coverslips were fixed with 4% paraformaldehyde for 10 min at room temperature, followed by washing with PBS. After permeabilizing with 0.1% Tween 20

for 5 min, the cells or frozen sections were incubated with a Nile red (1 µg/ml, 72485; Sigma) and DAPI (Sigma-Aldrich) dual staining solution for 10 min in dark. Images were taken by confocal microscopy (Leica TCS SP2 AOBS, Leica Microsystems, Buffalo Grove, IL).

Immunofluorescence staining

Kidney cryosections were fixed with 4% paraformalin fixing solution for 15 min at room temperature. HK-2 cells cultured on coverslips were fixed with cold methanol: acetone (1 : 1) for 15 min at room temperature, followed by blocking with 10% normal donkey serum in PBS. Slides were incubated with primary antibodies against anti-CB2 (ab45942; Abcam), anti-CB2 (sc-293188; santa cruz), anti-Fibronectin (F3648; Sigma), anti- α -SMA (ab5694; Abcam), anti- β -catenin (610154; BD Biosciences), anti-Active- β -catenin (4270s; Cell Signaling Technology), anti-PPAR α (A18252; ABclonal), anti-MAGL (ab228598; Abcam), anti-MAGL (sc-398942; santa cruz), anti-ADRP (ab52356; Abcam), anti-NCC (AB3553; Sigma-Aldrich), anti-AQP3 (ab125219; Abcam), anti-AQP1 (ab9566; Abcam), anti-E-cadherin (ab76055; Abcam), anti-Lotus Tetragonolobus Lectin (LTL) (FL-1321; VECTOR Laboratories), anti-Peanut Agglutinin (PNA) (FL-1071; VECTOR Laboratories), and anti-Dolichos Biflorus Agglutinin (DBA) (FL1031; VECTOR Laboratories). After washing with TBS-T, slides were incubated with Cy2 or Cy3-conjugated donkey anti-mouse or anti-rabbit IgG (Jackson ImmunoResearch Laboratories, West Grove, PA). Nuclei were stained with DAPI (Cat. C1006; Beyotime) according to the manufacturer's instructions. Images were captured using confocal microscopy (Leica TCS SP2 AOBS; Leica Microsystems, Buffalo Grove, IL).

Histology and immunohistochemical staining

Paraffin-embedded (3 μ m) mouse kidney sections were prepared using routine protocols. Sections were stained with Sirius red staining to identify collagen deposition. Some sections were stained with periodic acid-Schiff (PAS) (BA4080A; BASO). Immunohistochemical staining was performed using routine protocol. The primary antibodies used were as follows: anti-CPT1A (ab128568; Abcam), anti-fibronectin (F3648; Sigma), anti- β -catenin (610154; BD Biosciences) and anti-MAGL (ab228598; Abcam). Images were taken by a microscope DP 27 CCD camera (Olympus, Japan).

Quantifications of staining

Slides stained with Sirius red, immunohistochemical and immunofluorescence were observed at high magnification (x 400, x 1000) fields from randomly selected fields. Each section contained 10 fields, and the image of each part was divided into 100 squares. The tissue fibrosis stained in red was scored. Quantification of fibrotic lesions or positive area was assessed by the Image Pro plus software V6.0 (Media Cybernetics, Inc., Rockville, USA). The injury score was assessed by tubular dilation, hyaline casts and detached epithelial cells in tubular lumens as well as detached brush borders. The percentages of tubular injury in each image were calculated by three experienced observers in a blinded fashion.

LC-MS

Plasma pretreatment was conducted by melting the frozen samples on an ice surface and absorbing 200 μ l plasma. 10^7 cells were digested by pancreatic enzyme and then centrifuged at 4 $^{\circ}$ C and 800 rpm for 5 min. 200 μ l of toluene was added to the plasma and cell precipitates samples and the mixture were centrifuged for 10 min at 13000 rpm at 4 $^{\circ}$ C for 30 s after shock. The kidney tissue samples (weighing 20 mg) were pretreated by adding 200 μ l of toluene. The mixture was ground, crushed, and

then centrifuged at 13000 rpm at 4 °C for 10 min after shaking for 30 s. The upper organic phase was then transferred to a 1.5 ml EP tube and dried using a nitrogen blower. The residue was resolved by adding 200 µl of 75% methanol and vortexed for 30 s. The sample was then centrifuged at 14000 rpm at 4 °C for 20 min and subjected to LC-MS analysis. For all liquid chromatography-mass spectrometry (LC-MS) methods, LC-MS grade solvents were used. The standard reagents used were as follows: 2-AG (Item No.62160; Cayman Chemical); AEA (Catalog No.1339; Tocris Bioscience).

Transmission Electron Microscopy

Kidney cortex and HK-2 cells were fixed in 1.25% glutaraldehyde/0.1 M phosphate buffer, followed by resin embedding and ultrafine section making. Slides were subjected to assess kidney tubular mitochondrial ultrastructure and lipid droplets under an electron microscope (JEOL JEM - 1010, Tokyo, Japan).

ATP assay

ATP concentrations of HK-2 cells were assessed by enhanced ATP assay kit (S0027; Beyotime Biotechnology), according to the manufacturer's protocol.

Reverse transcription (RT) and real-time PCR

Total RNA was obtained using TRIzol RNA isolation system (Life Technologies, Grand Island, NY) according to the manufacturer's instruction.

Reverse transcription (RT) PCR was performed using HiScript III RT SuperMix for qPCR (R323-01; Vazyme, China). DNA was synthesized using 2 µg of RNA in 20 µl of reaction buffer containing 4 x

gDNA wiper mix and 5 × HiScript III qRT SuperMix.

Real-time PCR was performed on ABI PRISM 7000 Sequence Detection System (Applied Biosystems, Foster City, CA), using ChamQ SYBR qPCR Master Mix (High ROX Premixed) (Q341-02/03; Vazyme, China). The RNA levels of various genes were calculated after normalized by β-actin.

Transcriptomic analysis

RNA-seq was conducted to acquire the transcriptome of kidney tissues from various groups of mice. TRIzol reagent was utilized to extract total RNA, which was subsequently evaluated for RNA integrity using the RNA Nano 6000 Assay Kit of the Bioanalyzer 2100 system (Agilent Technologies, CA, USA). The total RNA served as input material for RNA sample preparations, with mRNA being purified from it using poly-T oligo-attached magnetic beads. Subsequently, cDNA was synthesized using the mRNA fragments as templates, and sequencing libraries were generated. The quality of the library was evaluated using the Agilent Bioanalyzer 2100 system, and the index-coded samples were clustered in accordance with the manufacturer's guidelines. Subsequently, the library preparations were sequenced on an Illumina Novaseq platform, generating 150 bp paired-end reads. The raw data, in fastq format, underwent initial processing via in-house perl scripts. The reference genome and gene model annotation files were obtained directly from the genome website. The reference genome's index was constructed through the utilization of Hisat2 v2.0.5, while the paired-end clean reads were aligned to the reference genome using the same software. The read numbers mapped to each gene were counted using FeatureCounts, and subsequently, the FPKM of each gene was computed based on the gene's length and the mapped read count. The DESeq2 R package (1.20.0) was employed to conduct differential expression analysis of two conditions/groups, each with two biological replicates. The clusterProfiler

R package was utilized to conduct Gene Ontology (GO) enrichment analysis on genes that were differentially expressed. Statistical enrichment of differential expression genes in KEGG pathways was tested using the same package. Reactome pathways were deemed significantly enriched by differential expressed genes if their corrected *P* value was less than 0.05. The local version of the GSEA analysis tool was employed to obtain GO, KEGG, Reactome, DO, and DisGeNET GSEA data sets.

Untargeted Metabolomics

Tissue samples were collected and prepared according to the manufacturer's instructions. UHPLC-MS/MS analyses were completed by an UHPLC (ThermoFisher, Germany) coupled with an Orbitrap Q ExactiveTM HF mass spectrometer (Thermo Fisher, Germany) in Novogene Co., Ltd. (Beijing, China). The raw data were processed by the Compound Discoverer 3.3 (CD3.3, ThermoFisher), including peak alignment, peak picking, and metabolite identification. The metabolite annotation was performed using the KEGG database, HMDB database and LIPIDMaps database. Pareto-scaled principal component analysis (PCA) and orthogonal partial least-squares discriminant analysis (OPLS-DA) were performed at meta X. Comparisons of metabolites were made by univariate analysis (t-test) between two groups. The metabolites with $VIP > 1$ and $P\text{-value} < 0.05$ and fold change ≥ 2 or $FC \leq 0.5$ were considered statistically significant. Volcano plots and the correlation between differential metabolites were analyzed by R package (ropis).

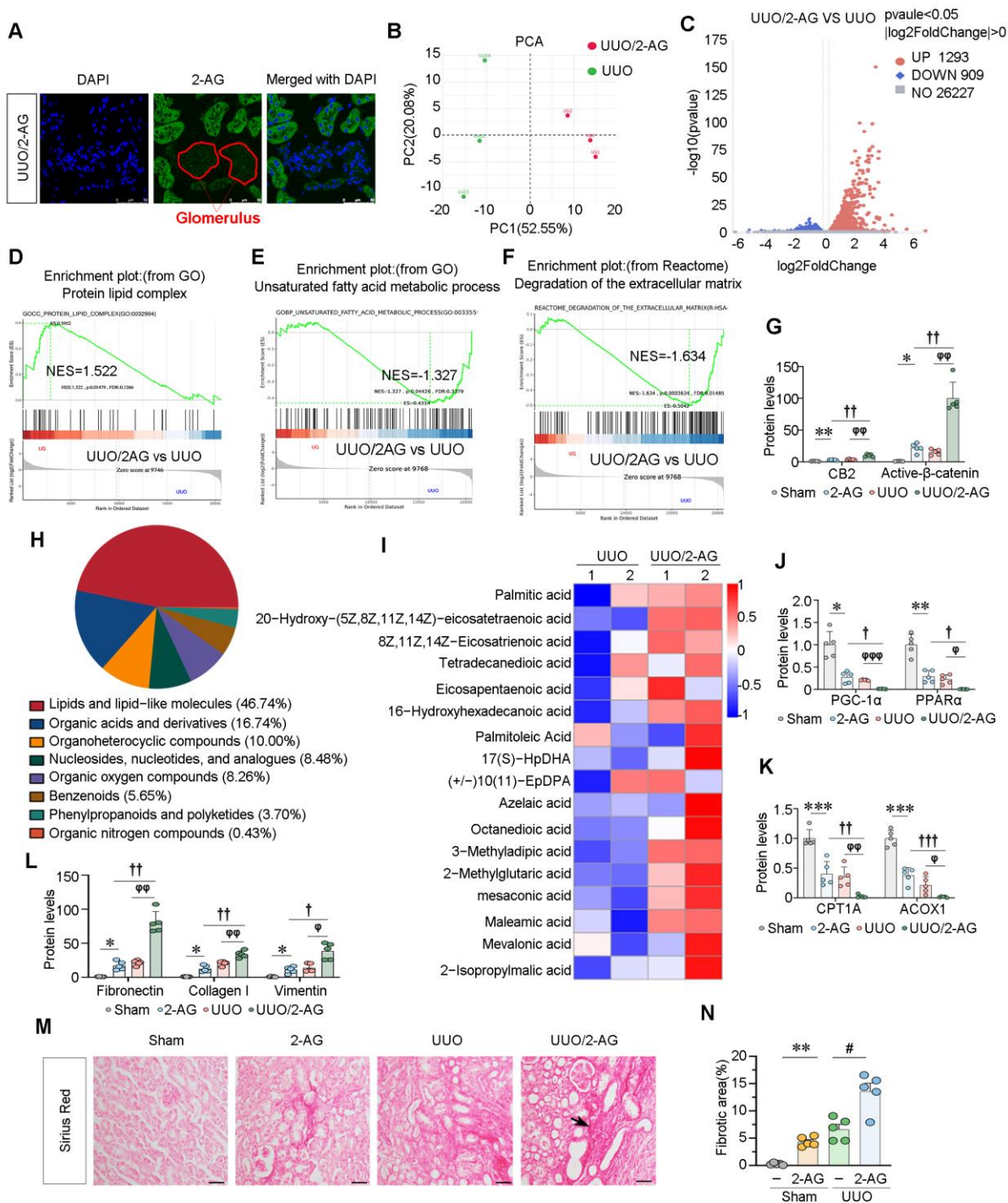
Statistical analyses

All data were expressed as mean with SEM. Statistical analysis of the data was carried out using IBM SPSS Statistics 25. The validity of assumptions included the normality of data, homogeneity of variance

and independence of observations was assessed before performing statistical tests. Non-parametric tests were used when the assumptions of the statistical approach were not satisfied. Chi-square test was used for the comparisons of two rates or two composition ratios. For the parametric analysis, comparisons were made by Student's t-test for comparison of two groups, or via one-way analysis of variance followed by the Least Significant Difference or Dunnett's T3 procedure for comparison of multiple groups. A value of $P < 0.05$ was considered statistically significant. Bivariate correlation analysis was performed using Pearson and Spearman rank correlation analysis.

References

1. Chen Z, Tu Y, Zhang D, Liu C, Zhou Y, Li X, et al. A thermosensitive nanoplatform for photoacoustic imaging and NIR light triggered chemo-photothermal therapy. *Biomater Sci.* 2020; 8: 4299-4307.
2. Li J, Niu J, Min W, Ai J, Lin X, Miao J, et, al. B7-1 mediates podocyte injury and glomerulosclerosis through communication with Hsp90ab1-LRP5- β -catenin pathway. *Cell Death Differ.* 2022; 29: 2399-2416.



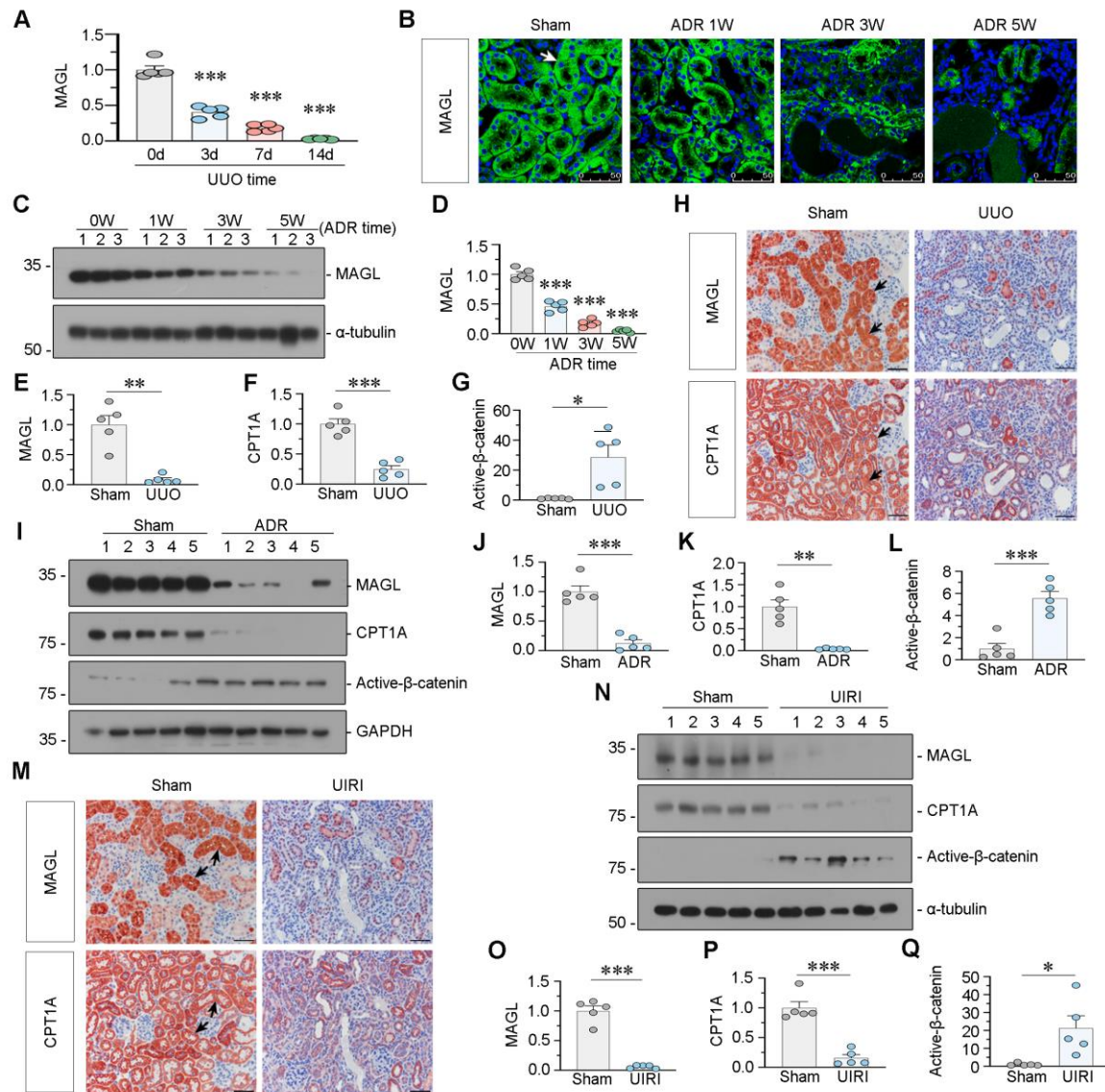
Supplementary Figure S1

315

316 **Supplementary Figure S1. 2-AG exacerbates renal fibrosis and lipid accumulation in UUO mice**

317 **A.** Representative micrographs showing the fluorescence of (indocyanine green)-2-AG in kidneys from UUO/2-AG mice. The
318 area circled by the red line indicates glomerulus. Scale bar, 50 μm. **B.** Representative graph showing the principal component
319 analysis (PCA) by RNA-seq in kidneys from UUO mice or UUO mice with intravenous injection of 2-AG. **C.** Volcano plot
320 showing the differentially expressed genes in 2 groups. **D-F.** Gene set enrichment analysis (GSEA) enrichment plots showing

the different enrichment of genes in UUO/2-AG mice compared to UUO alone mice. $P < 0.05$. NES: normalized enrichment score. **G.** Quantitative data showing renal Expression of CB2 and Active- β -catenin in different groups. $*P < 0.05$, $**P < 0.01$, versus the sham control group alone; $^{\dagger\dagger}P < 0.01$ versus the 2-AG group alone; $^{\varphi\varphi}P < 0.01$ versus the UUO group alone. $n = 5$. **H.** Representative pie chart showing how many superclasses have been identified based on metabonomics. **I.** Representative heatmap plot of metabonomics analysis showing the changes in medium, long as well as very long-chain fatty acids and their derivatives. **J-L.** Quantitative data showing renal expression of PGC-1 α , PPAR α , CPT1A, ACOX1, Fibronectin, Collagen I and Vimentin in different groups. $*P < 0.05$, $**P < 0.01$, $***P < 0.001$ versus the sham control group alone; $^{\dagger}P < 0.05$, $^{\dagger\dagger}P < 0.01$, $^{\dagger\dagger\dagger}P < 0.001$ versus the 2-AG group alone; $^{\varphi}P < 0.05$, $^{\varphi\varphi}P < 0.01$, $^{\varphi\varphi\varphi}P < 0.001$ versus the UUO group alone. $n = 5$. **M.** Representative micrographs showing the expression of fibrotic area in different groups. Arrow indicates positive staining. Scale bar, 50 μ m. **N.** Quantitative data showing quantification of fibrotic area. Kidney sections were subjected to Sirius Red staining. At least 10 randomly selected fields were evaluated under $400\times$ magnification and results were averaged for each animal. $**P < 0.01$ versus the sham control group alone; $^{\#}P < 0.05$ versus the UUO group alone. $n = 5$.

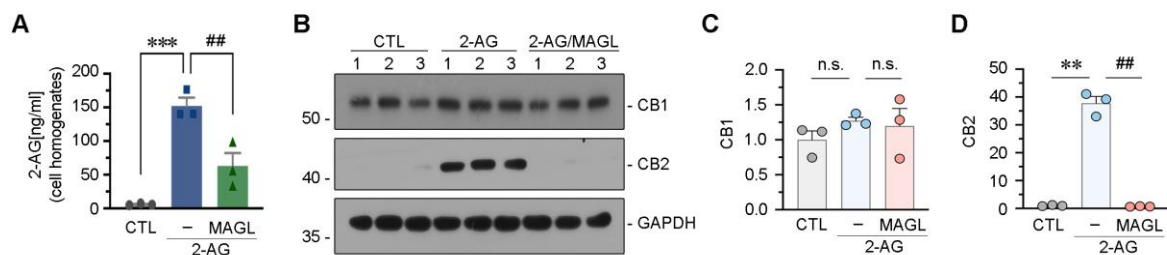


Supplementary Figure S2

Supplementary Figure S2. Loss of MAGL correlates with lipid accumulation and fibrosis

A. Quantitative data showing the expression of MAGL in different groups. Mice were sacrificed at different days after UUO surgery. Numbers (1 – 3) indicate each individual animal in a given group. $***P < 0.001$ versus the sham control group alone. $n = 5$. **B.** Representative immunofluorescence micrographs showing renal MAGL expression in different groups. Mice were sacrificed at different times after injection of ADR. White arrow indicates positive staining. Scale bar, 50 μm . **C-D.** Representative western blot and quantitative data showing the expression of MAGL in different groups. Numbers (1 – 3) indicate each individual animal in a given group. $***P < 0.001$ versus the sham group alone. $n = 5$. **E-G.** Quantitative data

showing the expression of MAGL, CPT1A and Active- β -catenin in UUO and sham mice. Numbers (1 – 5) indicate each individual animal in a given group. $*P < 0.05$, $**P < 0.01$, $***P < 0.001$ versus the sham control group alone. n = 5. **H.** Representative micrographs showing renal MAGL (top) and CPT1A (bottom) expression in UUO and sham mice. Black arrows indicate positive staining. Scale bar, 50 μ m. **I-L.** Representative western blot and quantitative data showing the expression of MAGL, CPT1A and Active- β -catenin in ADR and sham mice. Numbers (1 – 5) indicate each individual animal in a given group. $**P < 0.01$, $***P < 0.001$ versus the sham control group alone. n = 5. **M.** Representative micrographs showing renal MAGL (top) and CPT1A (bottom) expression in UIRI and sham mice. UIRI mice were sacrificed at 11 d after ischemia reperfusion surgery. Black arrows indicate positive staining. Scale bar, 50 μ m. **N-Q.** Representative western blot and quantitative data showing the expression of MAGL, CPT1A and Active- β -catenin in UIRI and sham mice. Numbers (1 – 5) indicate each individual animal in a given group. $*P < 0.05$, $***P < 0.001$ versus the sham control group alone. n = 5.

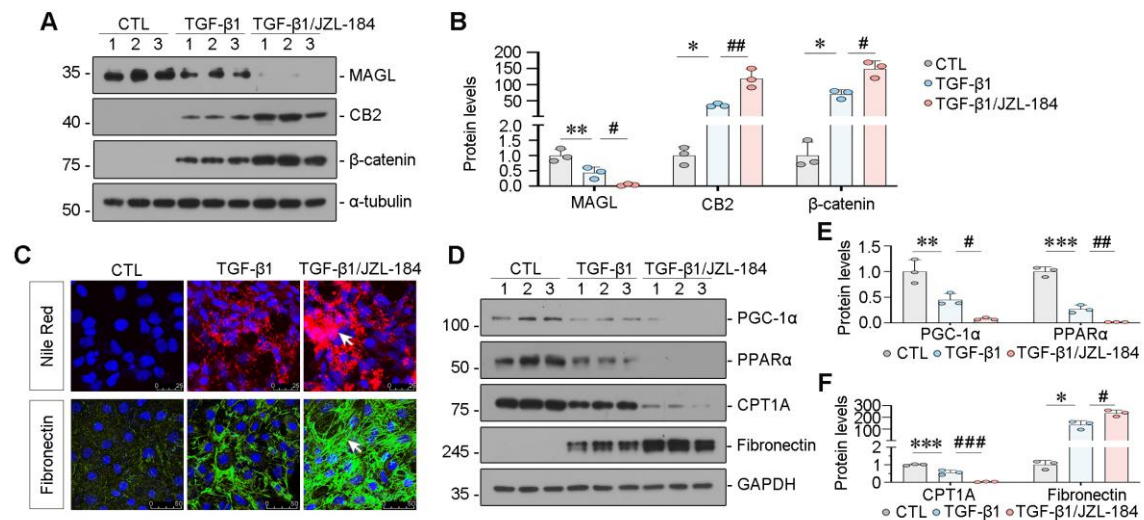


Supplementary Figure S3

Supplementary Figure S3. MAGL reduces 2-AG levels and inhibits CB2 expression in vitro

A. Representative graph showing 2-AG levels in cell homogenates in different groups by LC/MS analysis. HK-2 cells were pretreated with recombinant MAGL protein (100 ng/ml) for 1 h, and then treated with 2-AG (100 μ M) for 24 h. $***P < 0.001$ versus the control group alone. $##P < 0.01$ versus 2-AG treatment group alone. **B-D.** Representative western blot and quantitative data showing the expression of CB1 and CB2 in different groups. Numbers (1 – 3) indicate each individual culture

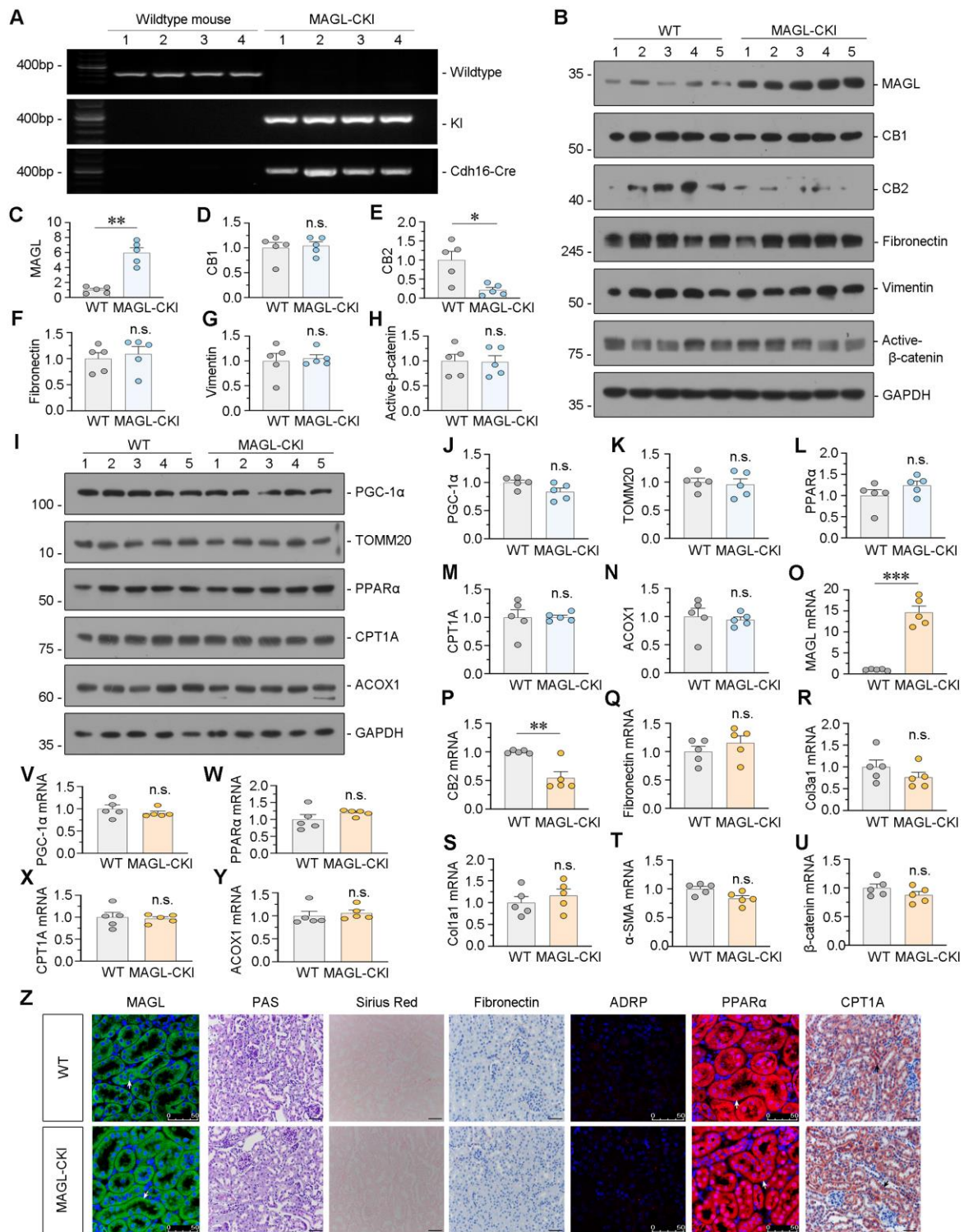
in a given group. n.s., $^{**}P < 0.01$ versus the control group alone. n.s., $^{##}P < 0.01$ versus 2-AG treatment group alone. n.s.: none of significance. n = 3.



Supplementary Figure S4

Supplementary Figure S4. MAGL inhibitor exacerbates TGF-β1-induced lipotoxicity and fibrosis in renal tubular cells

A-B. Representative western blot and quantitative data showing the expression of MAGL, CB2 and β-catenin in different groups. HK-2 cells were treated with TGF-β1 (5 ng/ml) alone or cotreated with JZL-184 (20 μmol/ml) for 24 h. $^{*}P < 0.05$, $^{**}P < 0.01$ versus the control group alone; $^{#}P < 0.05$, $^{##}P < 0.01$ versus the TGF-β1 treatment group alone. n = 3. **C.** Representative immunofluorescence micrographs showing the expression of lipid (Nile Red) and Fibronectin in different groups. White arrows indicate positive staining. For Nile Red staining, scale bar, 25 μm; For Fibronectin, scale bar, 50 μm. **D-F.** Representative western blot and quantitative data showing the expression of PGC-1α, PPARα, CPT1A and Fibronectin in different groups. $^{*}P < 0.05$, $^{**}P < 0.01$, $^{***}P < 0.001$ versus the control group alone; $^{#}P < 0.05$, $^{##}P < 0.01$, $^{###}P < 0.001$ versus the TGF-β1 treatment group alone. n = 3.

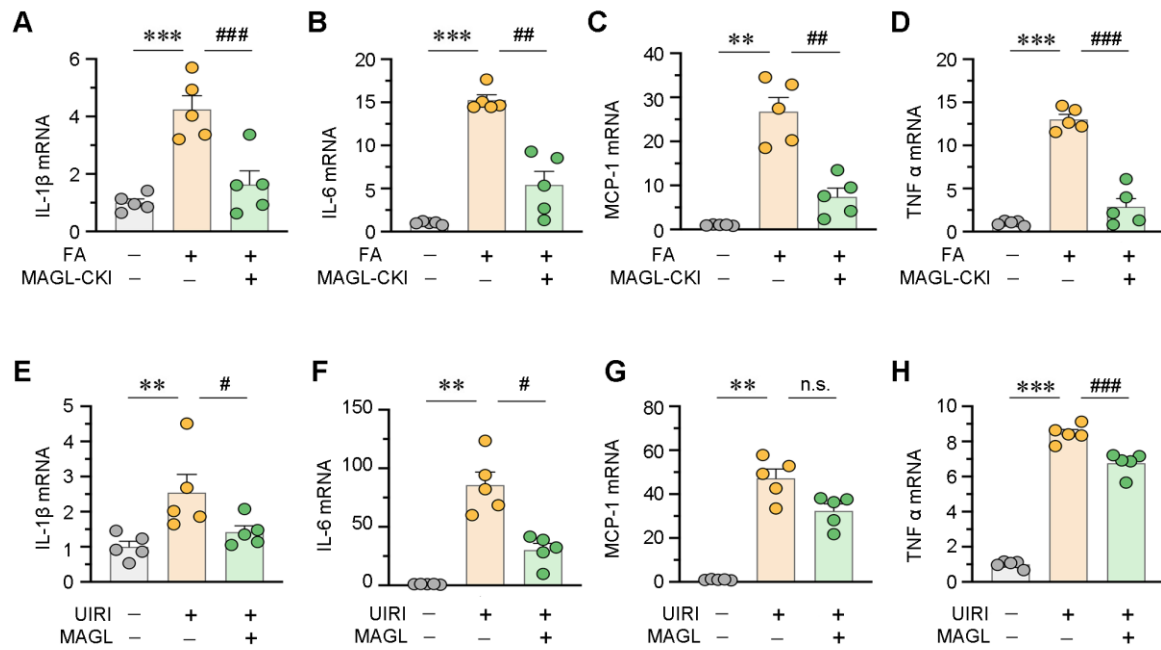


Supplementary Figure S5

Supplementary Figure S5. MAGL gene knock-in does not affect renal lipid accumulation, mitochondrial dysfunction, and fibrosis

A. Representative PCR analysis showing genotyping identification of tubular cell specific MAGL knock-in mice (Rosa26-

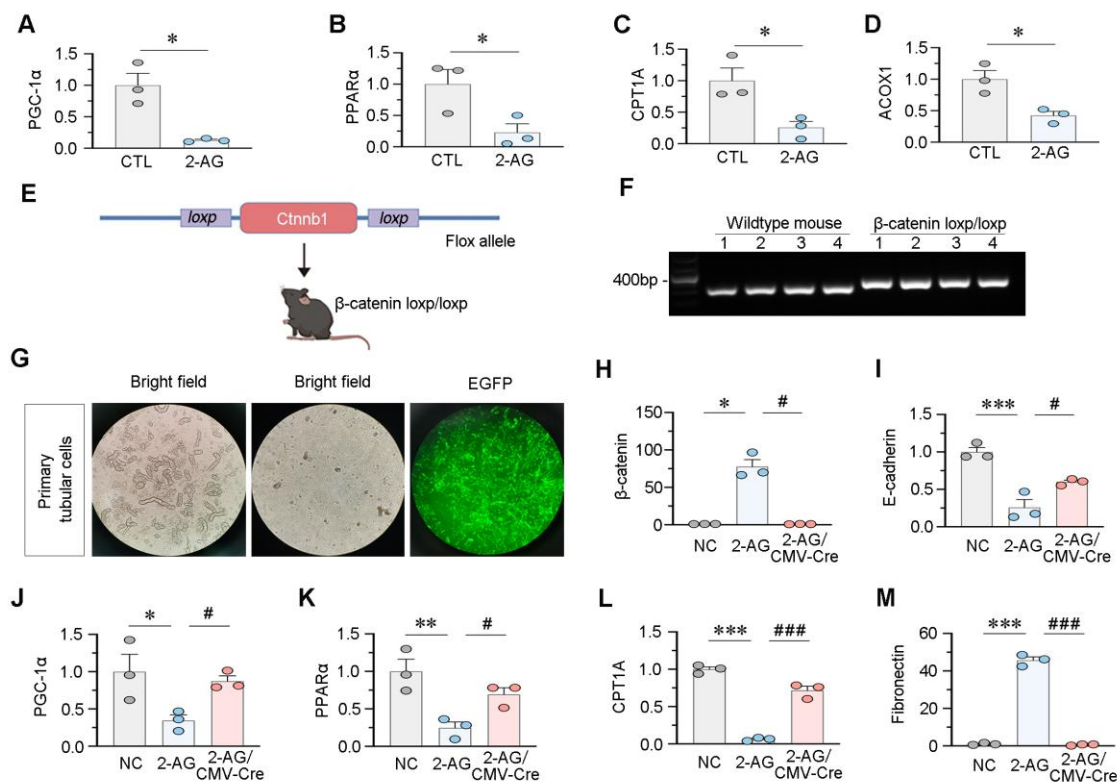
379 MAGL-CKI). **B-H.** Representative western blot and quantitative data showing the expression of MAGL, CB1, CB2,
380 Fibronectin, Vimentin and Active- β -catenin in wildtype and MAGL-CKI mice. Numbers (1 – 5) indicate each individual
381 animal in a given group. n.s., $*P < 0.05$, $**P < 0.01$ versus the wildtype control group alone. n = 5. n.s.: none of significance.
382 **I-N.** Representative western blot and quantitative data showing the expression of PGC-1 α , TOMM20, PPAR α , CPT1A and
383 ACOX1 in wildtype and MAGL-CKI mice. Numbers (1 – 5) indicate each individual animal in a given group. n.s. versus the
384 wildtype control group alone. n = 5. n.s.: none of significance. **O-Y.** Quantitative data showing the mRNA level of MAGL,
385 CB2, Fibronectin, Col3a1, Col1a1, α -SMA, β -catenin, PGC-1 α , PPAR α , CPT1A and ACOX1 in wildtype and MAGL-CKI
386 mice. n.s., $**P < 0.01$, $***P < 0.001$ versus the wildtype control group alone. n = 5. n.s.: none of significance. **Z.** Representative
387 micrographs showing renal expression of MAGL, Fibronectin, ADPR, PPAR α , CPT1A and PAS, Sirius Red staining in 2
388 groups. Arrows indicate positive staining. Scale bar, 50 μ m.
389



Supplementary Figure S7

Supplementary Figure S7. MAGL protects against inflammation

A-D. Quantitative data showing renal mRNA levels of IL- β , IL-6, MCP-1 and TNF- α in different groups. ** P < 0.01, *** P < 0.001 versus the wildtype control group alone; ## P < 0.01, ### P < 0.001 versus the FA treatment group alone. n = 5. **E-H.** Quantitative data showing renal mRNA levels of IL- β , IL-6, MCP-1 and TNF- α in different groups. ** P < 0.01, *** P < 0.001 versus the wildtype control group alone; n.s., # P < 0.05, ### P < 0.001 versus the UIRI group alone. n = 5. n.s.: none of significance.



Supplementary Figure S8

Supplementary Figure S8. 2-AG suppresses PPARα/PGC-1α-mediated FAO via β-catenin signaling

A-D. Quantitative data showing the expression of PGC-1α, PPARα, CPT1A and ACOX1 in 2 groups. HK-2 cells were treated with 2-AG for 24 h. * $P < 0.05$ versus the control group alone. $n = 3$. **E-F.** Representative graph showing establishment of β-catenin loxp/lox mice. Genotyping was confirmed by PCR analysis. **G.** Representative micrographs showing the bright field and fluorescence field (EGFP) in primarily cultured tubular cells from β-catenin loxp/lox mice (under $100 \times$ magnification). The cells were transfected with Adv-CMV-Cre or Adv-NC virus and then treated with 2-AG (100 μM). **H-M.** Quantitative data showing the expression of β-catenin, E-cadherin, PGC-1α, PPARα, CPT1A and Fibronectin in different groups. * $P < 0.05$, ** $P < 0.01$, *** $P < 0.001$ versus the Adv-NC group alone; # $P < 0.05$, ### $P < 0.001$ versus the Adv-NC+2-AG group alone. $n = 3$.

Supplementary table S1.**Clinical sample source: Serum samples from healthy individuals and CKD patients****Healthy individuals**

No.	Gender	Age
1	M	28
2	M	19
3	M	22
4	M	20
5	M	21
6	M	29
7	M	30
8	M	19
9	M	25
10	M	19
11	M	26
12	M	26
13	M	29
14	M	23
15	M	29
16	M	27
17	M	27
18	M	19
19	M	29
20	M	25
21	M	27
22	M	27
23	M	26
24	M	26
25	M	29
26	M	26
27	M	23
28	M	19
29	M	24
30	F	26
31	F	27
32	F	33
33	F	27
34	F	26

CKD patients at 5 stage

No.	Gender	Age	eGFR(ml/min/1.73m ²)
1	F	58	5.00
2	F	54	6.18

3	M	24	3.62
4	F	56	7.17
5	F	62	6.55
6	M	57	8.95
7	M	29	6.23
8	M	33	9.25
9	F	75	3.90
10	M	40	7.82
11	M	45	7.61
12	F	37	9.37
13	F	41	3.76
14	F	32	5.45
15	M	49	9.46
16	F	54	12.05
17	M	41	5.75
18	M	67	12.65
19	F	57	7.98
20	M	36	4.32
21	M	45	14.95
22	M	69	9.32
23	M	53	8.15
24	M	54	5.01
25	M	33	3.76
26	M	73	3.80
27	M	32	8.14
28	M	41	6.82
29	M	23	9.68
30	M	36	4.87
31	F	70	6.34
32	M	51	12.71
33	F	59	9.34
34	M	53	5.97
35	M	67	14.89
36	F	51	5.10
37	F	62	5.99
38	M	59	7.83
39	M	51	5.20
40	M	37	6.12
41	M	31	5.30
42	M	75	7.61
43	M	52	6.03
44	M	49	12.07

Supplementary table S2.

Clinical sample source: Renal biopsy tissue samples from CKD patients

CKD patients

No.	G stage	Gender	Age	eGFR(ml/min/1.73m ²)
1	CKD 1	F	28	129.08
2	CKD 1	F	51	91.13
3	CKD 1	F	27	121.99
4	CKD 1	F	47	108.57
5	CKD 1	F	48	108.49
6	CKD 1	M	25	126.95
7	CKD 1	F	22	126.35
8	CKD 1	F	27	140.63
9	CKD 1	M	40	112.88
10	CKD 1	M	41	108.31
11	CKD 1	M	24	108.43
12	CKD 1	F	44	108.26
13	CKD 1	F	24	130.95
14	CKD 1	F	39	92.43
15	CKD 1	F	57	103.17
16	CKD 1	F	29	120.29
17	CKD 1	M	24	123.41
18	CKD 1	M	35	101.79
19	CKD 1	F	48	110.63
20	CKD 1	F	25	107.44
21	CKD 1	M	50	107.83
22	CKD 1	F	49	97.68
23	CKD 1	M	22	105.49
24	CKD 1	F	28	111.1
25	CKD 1	F	42	106.61
26	CKD 1	F	43	115.37
27	CKD 1	M	45	102.1
28	CKD 1	F	36	113.23
29	CKD 1	F	23	90.9
30	CKD 1	F	34	116.14
31	CKD 1	F	29	121.71
32	CKD 1	F	40	110.71
33	CKD 1	M	48	94.25
34	CKD 1	M	36	112.18
35	CKD 2	F	53	66.26
36	CKD 2	F	40	83.21
37	CKD 2	F	50	81.38
38	CKD 2	M	40	63.49
39	CKD 2	M	55	88.45

40	CKD 2	M	34	72.65
41	CKD 2	M	64	76.46
42	CKD 2	M	28	81.87
43	CKD 2	F	57	88.97
44	CKD 2	M	50	72.63
45	CKD 2	M	63	89.98
46	CKD 2	F	70	89.17
47	CKD 2	F	35	76.47
48	CKD 2	F	33	86.05
49	CKD 2	F	33	77.55
50	CKD 2	M	53	75.52
51	CKD 2	F	58	76.93
52	CKD 2	F	41	80.1
53	CKD 2	F	28	83.89
54	CKD 2	M	45	63.17
55	CKD 2	M	33	81.84
56	CKD 2	F	51	68.34
57	CKD 2	M	63	71.28
58	CKD 3	F	50	48.26
59	CKD 3	M	46	36.68
60	CKD 3	F	25	34.38
61	CKD 3	F	44	55.6
62	CKD 3	M	38	50.98
63	CKD 3	F	18	39.22
64	CKD 3	M	44	32.2
65	CKD 3	F	48	48.43
66	CKD 3	M	68	40.63
67	CKD 3	M	38	52.7
68	CKD 3	M	45	57.3
69	CKD 3	M	37	43.11
70	CKD 3	F	48	41.37
71	CKD 3	F	22	41.17
72	CKD 3	F	35	48.44
73	CKD 3	F	41	56.14
74	CKD 3	F	47	51.47
75	CKD 3	M	55	39.09
76	CKD 4	M	56	26.45
77	CKD 4	M	48	21.89
78	CKD 4	M	49	23.88
79	CKD 4	F	67	27.19
80	CKD 4	M	32	17.45
81	CKD 4	F	34	23.74
82	CKD 4	M	45	25.75

83	CKD 5	M	51	13.33
84	CKD 5	M	54	2.61
85	CKD 5	M	38	6.21
86	CKD 5	M	59	4.66
87	CKD 5	F	50	5.32
88	CKD 5	M	56	8.32
89	CKD 5	M	83	11.66

Data used in Figure 3D & F; Figure 4D, G, H & I. F = Female; M = Male.

Supplementary table S3.

Clinical sample source: Urine samples from healthy individuals and CKD patients

Healthy individuals

No.	Gender	Age	Urinary MAGL (pg/mg)
1	F	26	341.0221632
2	F	33	894.642131
3	F	27	307.6385853
4	F	27	1081.704609
5	F	25	729.7321049
6	M	26	171.7834208
7	M	25	211.152718
8	M	25	311.3286571
9	M	28	142.6557255
10	F	24	129.3172601
11	F	27	504.9118286
12	F	30	154.9712778
13	F	24	150.0778726

CKD patients

No.	G stage	Gender	Age	eGFR(ml/min/1.73m ²)	Urinary MAGL (pg/mg)
1	CKD1	M	56	98.6	180.5193846
2	CKD1	F	47	105.4	6.104819106
3	CKD1	M	58	98.9	38.92618539
4	CKD1	M	48	97	39.54730818
5	CKD1	F	42	115.4	57.66846939
6	CKD1	M	63	96	20.82221815
7	CKD1	F	30	140.2	93.97456132
8	CKD1	F	47	105.4	91.10808055
9	CKD1	F	48	104.1	10.58855424
10	CKD1	F	52	97.5	38.95054793
11	CKD1	F	30	113.8	126.8174145
12	CKD1	F	21	129.5	38.05877534
13	CKD1	M	59	98.8	92.42660399

14	CKD1	M	46	109.5	81.71865385
15	CKD1	M	28	105.4	191.1578822
16	CKD1	M	22	123.1	154.480524
17	CKD1	M	43	100.5	60.46820352
18	CKD1	M	33	115.2	31.53836225
19	CKD1	M	48	94.2	68.35892165
20	CKD1	F	27	134.9	62.85161791
21	CKD1	F	64	96.4	114.9032194
22	CKD1	M	32	118.7	104.4532898
23	CKD1	M	46	105.2	76.96246288
24	CKD1	M	52	101.4	139.653226
25	CKD1	F	28	111.1	195.6812191
26	CKD1	M	45	109	137.3971158
27	CKD1	M	59	93.4	139.7311148
28	CKD1	F	34	110.6	42.53133655
29	CKD1	M	53	103	74.82220467
30	CKD1	M	44	106.6	44.35704113
31	CKD1	F	29	150.2	70.2072238
32	CKD1	F	17	135.7	104.8414661
33	CKD1	M	34	114.4	125.2002836
34	CKD1	F	27	134.9	149.5767598
35	CKD1	M	54	98.9	84.85976672
36	CKD1	F	49	106.4	87.05654941
37	CKD1	M	20	92.9	191.2244017
38	CKD1	M	26	135.7	147.2203605
39	CKD1	M	32	125.61	45.97638638
40	CKD2	M	48	89.1	118.7693769
41	CKD2	M	23	69.5	66.00569934
42	CKD2	F	51	68.3	127.6083514
43	CKD2	F	60	66	128.2346678
44	CKD2	M	28	80	35.80706494
45	CKD2	M	48	71.1	146.6034884
46	CKD2	F	52	60.9	80.62339517
47	CKD2	M	62	78.6	114.6808148
48	CKD2	M	34	79.4	24.08131631
49	CKD2	F	50	84.1	41.61903657
50	CKD2	F	28	60.8	138.3744988
51	CKD2	M	31	61.49	53.22295559
52	CKD2	M	41	63.05	61.55483988
53	CKD2	M	26	63.69	186.6606866
54	CKD2	M	57	68.34	8.036696247
55	CKD3	M	53	51.3	10.62484576
56	CKD3	F	44	40.3	16.00972937

57	CKD3	M	41	44.1	22.49448359
58	CKD3	F	61	34.6	58.43535525
59	CKD3	M	29	53.9	56.2131169
60	CKD3	F	53	36.9	34.35742308
61	CKD3	F	47	46.8	101.1871965
62	CKD3	F	58	48.2	122.3472384
63	CKD3	M	65	35.41	12.19461301
64	CKD3	F	58	36.86	193.8363425
65	CKD3	M	41	38.62	69.28638943
66	CKD3	M	52	39.36	48.51889749
67	CKD3	M	50	47.24	88.37050972
68	CKD3	M	54	47.9	13.42528568
69	CKD3	M	54	48.72	20.9967715
70	CKD3	M	76	48.99	38.65661369
71	CKD3	M	53	53.17	17.34653249
72	CKD3	M	54	54.3	99.81519059
73	CKD3	M	74	56.05	42.51611457
74	CKD3	M	66	58.65	112.9020511
75	CKD4	M	38	18.1	38.89501871
76	CKD4	F	31	28	77.26630048
77	CKD4	M	34	24.9	47.28028134
78	CKD4	M	48	15.96	30.97381583
79	CKD4	F	39	16.93	97.84359516
80	CKD4	F	39	20.08	46.11492229
81	CKD4	M	67	22.17	12.88928334
82	CKD4	F	55	23.2	46.68841113
83	CKD4	F	53	26.84	45.67943039
84	CKD4	M	78	27.92	48.02196528
85	CKD4	M	28	28.74	30.9668033
86	CKD4	M	72	28.75	39.64988151
87	CKD5	M	35	14.4	21.7809338
88	CKD5	F	58	3.36	98.28285494
89	CKD5	M	54	3.8	28.00405774
90	CKD5	M	70	4.72	45.88592914
91	CKD5	M	36	4.84	37.66568841
92	CKD5	M	29	5.11	86.72366017
93	CKD5	M	59	5.57	62.17962851
94	CKD5	M	63	5.57	36.494151
95	CKD5	F	36	6	13.62214403
96	CKD5	M	45	6.08	59.45721339
97	CKD5	M	40	7.12	12.75576065
98	CKD5	M	56	7.37	3.62017063
99	CKD5	F	51	7.6	101.2239338

100	CKD5	M	40	7.72	48.69562757
101	CKD5	M	37	7.79	37.32577402
102	CKD5	M	51	8.35	68.53457566
103	CKD5	M	25	8.81	6.067609929
104	CKD5	M	37	8.94	127.0484867
105	CKD5	M	57	9.02	71.47779154
106	CKD5	M	35	9.27	58.61299195
107	CKD5	M	30	9.85	22.19649102
108	CKD5	M	56	10.26	20.04661621

Data used in Figure 3E & G. F = Female; M = Male.

Supplementary table S4.

Nucleotide sequences of the primers used for RT-PCR or real-time PCR

Gene	Primer Sequence 5' to 3'	
	Forward	Reverse
CB2-mouse	TATGCTGGTTCCCTGCACTG	GAGCGAATCTCTCCACTCCG
MAGL-mouse	AGGCGAACTCCACAGAATGTT	ACAAAAGAGGTACTGTCCGTCT
PGC-1 α -mouse	AGTCCCATACACAACCGCAG	CCCTTGGGGTTCATTTGGTGA
PPAR α -mouse	TGCAAACCTTGGACTTGAACG	GATCAGCATCCCGTCTTTGT
CPT1A-mouse	GGTCTTCTCGGGTCGAAAGC	TCCTCCCACCAGTCACTCAC
ACOX1-mouse	CTTGGATGGTAGTCCGGAGA	TGGCTTCGAGTGAGGAAGTT
CPT2-mouse	CAATGAGGAAACCCTGAGGA	GATCCTTCATCGGGAAGTCA
ACOX2-mouse	TACCAACGCCTGTTTGAGTG	TTCCAGCTTTGCATCAGTG
Fibronectin-mouse	ATGTGGACCCCTCCTGATAGT	GCCCAGTGATTTCAGCAAAGG
Col3a1-mouse	CTGTAACATGGAAACTGGGGA AA	CCATAGCTGAACTGAAAACCAC C
Col1a1-mouse	GCTCCTCTTAGGGGCCACT	CCACGTCTCACCATTGGGG
α -SMA-mouse	GTCCCAGACATCAGGGAGTAA	TCGGATACTTCAGCGTCAGGA
β -catenin-mouse	ATGGAGCCGGACAGAAAAGC	CTTGCCACTCAGGGAAGGA
IL-1 β -mouse	AACCTTTGACCTGGGCTGTC	AAGGTCCACGGGAAAGACAC
IL-6-mouse	AGGAGACTTCACAGAGGATAC CA	TTCCACGATTTCACAGAGAACAT

MCP-1	CCCACTCACCTGCTGCTAC	TTCTTGGGGTCAGCACAGA
TNF- α	TCGTAGCAAACCACCAAGTG	CCTTGAAGAGAACCTGGGAG
β -actin-mouse	CAGCTGAGAGGGGAAATCGTG	CGTTGCCAATAGTGATGACC